



TECHNICAL REPORT RDMR-WD-10-15

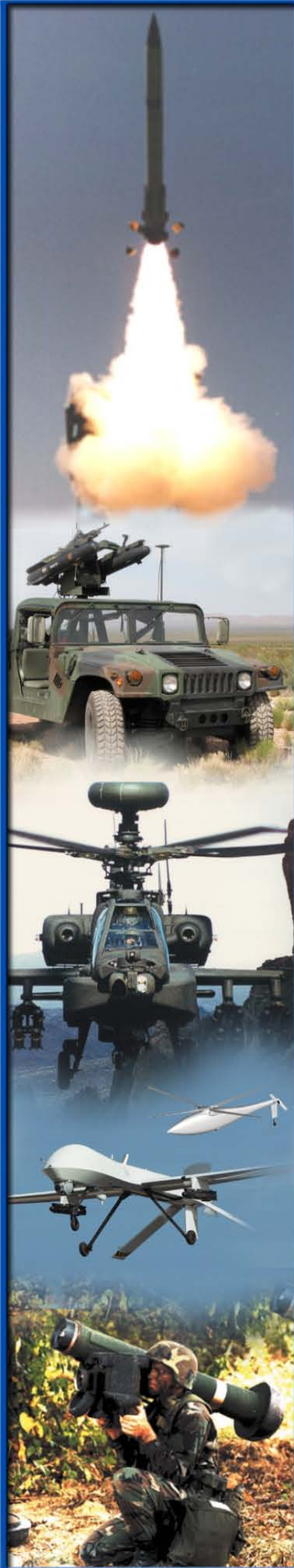
# THE DEVELOPMENT OF THE WALL MOMENTUM EROSIVE BURNING SCALING LAW AND MACRO SCALE EROSIVE BURNING MODEL

**Brian A. McDonald**

**Weapons Development and Integration Directorate  
Aviation and Missile Research, Development,  
and Engineering Center**

May 2010

Approved for public release, distribution is unlimited.



## **DESTRUCTION NOTICE**

**FOR CLASSIFIED DOCUMENTS, FOLLOW THE PROCEDURES IN DoD 5200.22-M, INDUSTRIAL SECURITY MANUAL, SECTION II-19 OR DoD 5200.1-R, INFORMATION SECURITY PROGRAM REGULATION, CHAPTER IX. FOR UNCLASSIFIED, LIMITED DOCUMENTS, DESTROY BY ANY METHOD THAT WILL PREVENT DISCLOSURE OF CONTENTS OR RECONSTRUCTION OF THE DOCUMENT.**

## **DISCLAIMER**

**THE FINDINGS IN THIS REPORT ARE NOT TO BE CONSTRUED AS AN OFFICIAL DEPARTMENT OF THE ARMY POSITION UNLESS SO DESIGNATED BY OTHER AUTHORIZED DOCUMENTS.**

## **TRADE NAMES**

**USE OF TRADE NAMES OR MANUFACTURERS IN THIS REPORT DOES NOT CONSTITUTE AN OFFICIAL ENDORSEMENT OR APPROVAL OF THE USE OF SUCH COMMERCIAL HARDWARE OR SOFTWARE.**

<b>REPORT DOCUMENTATION PAGE</b>			Form Approved OMB No. 074-0188	
Public reporting burden for this collection of information is estimated to average 1 hour per response, including the time for reviewing instructions, searching existing data sources, gathering and maintaining the data needed, and completing and reviewing this collection of information. Send comments regarding this burden estimate or any other aspect of this collection of information, including suggestions for reducing this burden to Washington Headquarters Services, Directorate for Information Operations and Reports, 1215 Jefferson Davis Highway, Suite 1204, Arlington, VA 22202-4302, and to the Office of Management and Budget, Paperwork Reduction Project (0704-0188), Washington, DC 20503				
1. AGENCY USE ONLY		2. REPORT DATE May 2010	3. REPORT TYPE AND DATES COVERED Final	
4. TITLE AND SUBTITLE The Development of the Wall Momentum Erosive Burning Scaling Law and Macro Scale Erosive Burning Model			5. FUNDING NUMBERS	
6. AUTHOR(S) Brian A. McDonald				
7. PERFORMING ORGANIZATION NAME(S) AND ADDRESS(ES) Commander, U.S. Army Research, Development, and Engineering Command ATTN: RDMR-WDP-M Redstone Arsenal, AL 35898			8. PERFORMING ORGANIZATION REPORT NUMBER  TR-RDMR-WD-10-15	
9. SPONSORING / MONITORING AGENCY NAME(S) AND ADDRESS(ES)			10. SPONSORING / MONITORING AGENCY REPORT NUMBER	
11. SUPPLEMENTARY NOTES				
12a. DISTRIBUTION / AVAILABILITY STATEMENT Approved for public release; distribution is unlimited.			12b. DISTRIBUTION CODE  A	
13. ABSTRACT ( <i>Maximum 200 Words</i> ) The traditional approach to erosive burning modeling in solid propellants is to correlate test data to bulk flow quantities such as Mach Number or velocity. Within certain flow regimes and for a fixed geometry the test data appears to correlate well with these variables, showing that the erosive burning magnitude is highly dependent upon the cross-flow velocity. However, erosive burning is well known to demonstrate a dependency upon the base burning rate of the propellant, as well as exhibiting a threshold cross-flow velocity condition, below which no apparent increase in burning rate is seen. Presented in this report are numerical results that demonstrate the erosive burning threshold condition and a correlation of the data to a quantity termed the wall momentum ratio. This ratio is based on the local wall shear stress and the local mass injection rate. The numerical results and the correlation are compared to test data obtained through ultrasound measurements of the propellant surface regression rate. The comparison shows excellent agreement with test data in both the burn rate augmentation factors and the threshold condition. The wall momentum function is used to develop a macro scale erosive burning model suitable for use in interior ballistics analyses as a predictive tool.				
14. SUBJECT TERMS Interior Ballistics, Solid Propellant, Erosive Burning, Modeling			15. NUMBER OF PAGES 58	
			16. PRICE CODE	
17. SECURITY CLASSIFICATION OF REPORT UNCLASSIFIED	18. SECURITY CLASSIFICATION OF THIS PAGE UNCLASSIFIED	19. SECURITY CLASSIFICATION OF ABSTRACT UNCLASSIFIED	20. LIMITATION OF ABSTRACT SAR	

NSN 7540-01-280-5500

Standard Form 298 (Rev. 2-89)  
Prescribed by ANSI Std. Z39-18  
298-102

## TABLE OF CONTENTS

	<u>Page</u>
<b>I. INTRODUCTION .....</b>	<b>1</b>
<b>II. BACKGROUND .....</b>	<b>2</b>
<b>III. MODEL DESCRIPTION .....</b>	<b>6</b>
<b>A. Overview of Numerical Simulation Code .....</b>	<b>6</b>
<b>B. Governing Equations .....</b>	<b>6</b>
<b>C. Gas Phase Boundary Conditions .....</b>	<b>7</b>
<b>D. Thermal Transport Model .....</b>	<b>8</b>
<b>E. Gas-Solid Interface .....</b>	<b>8</b>
<b>F. Finite Rate Chemistry Model .....</b>	<b>9</b>
<b>G. Model Definition and Boundary Conditions .....</b>	<b>9</b>
<b>IV. DEVELOPMENT OF THE WALL MOMENTUM FUNCTION .....</b>	<b>11</b>
<b>A. General Discussion and Test Data .....</b>	<b>11</b>
<b>B. Numerical Modeling of a High Burn Rate-High Shear Geometry .....</b>	<b>12</b>
<b>C. Numerical Modeling of the 5-Inch Test Article .....</b>	<b>25</b>
<b>D. Wall Momentum Ratio Definition .....</b>	<b>27</b>
<b>E. Examination of Threshold Condition .....</b>	<b>29</b>
<b>F. Wall Momentum Applied to Test Data .....</b>	<b>30</b>
<b>G. Integral Scaling of Wall Momentum .....</b>	<b>32</b>
<b>H. Observation of the Wall Momentum Function .....</b>	<b>34</b>
<b>V. WALL MOMENTUM RATIO MACRO MODEL FOR INTERIOR BALLISTICS .....</b>	<b>35</b>
<b>A. Development of the Wall Momentum Macro Correlation .....</b>	<b>36</b>
<b>B. Macro Model Validation .....</b>	<b>40</b>
<b>C. Observations and Conclusions on the Wall Momentum Macro Model .....</b>	<b>44</b>
<b>VI. CONCLUSIONS .....</b>	<b>45</b>
<b>REFERENCES .....</b>	<b>47</b>
<b>NOMENCLATURE .....</b>	<b>49</b>

## LIST OF ILLUSTRATIONS

<u>Figure</u>	<u>Title</u>	<u>Page</u>
1.	Window Bomb Strand Burner .....	2
2.	Measured Chamber Pressure .....	3
3.	5-Inch CP Augmentation Factor Data .....	11
4.	Schematic of Computational Domain .....	12
5.	Near-Wall Temperature Profile .....	14
6.	Temperature Profiles Out to Thermal Boundary Layer Edge.....	15
7.	Comparison of the AP Decomposition and APd-Binder Flame Thicknesses for $M=0.0$ .....	16
8.	APd-Binder Flame Thickness Comparison for Various Free-Stream Mach Numbers.....	17
9.	AP Decomposition Flame Thickness Comparison for Various Free-Stream Mach Numbers.....	18
10.	Near-Wall Vorticity for Various Free-Stream Mach Numbers .....	19
11.	APd-Binder Flame and Vorticity for $M=0.8$ .....	20
12.	Near-Wall Tangential Velocity Profiles.....	21
13.	Comparison of Reaction Rate Gradients to Thermal Gradients .....	22
14.	Comparison of Thermal Gradients at the Solid-Gas Interface for a High Rate and Low Rate Propellant.....	23
15.	Interior Ballistics Results with Finite and Infinite Rate Models.....	24
16.	Erosive Burning Rate Compared to the Base Rate .....	25
17.	Comparison of Numerical Augmentation Factors to Ultrasound Test Data .....	26
18.	Numerical Augmentation Factor Versus Wall Momentum Ratio .....	28
19.	$M=0.01$ Resultant Velocity Vectors.....	29
20.	$M=0.1$ Resultatn Velocity Vectors.....	29

## LIST OF ILLUSTRATIONS (CONT)

<u>Figure</u>	<u>Title</u>	<u>Page</u>
21.	Calculated $\lambda$ Function Versus Mach Number.....	30
22.	EBT Test Data Augmentation Factor's Versus Derived $\lambda$ Function .....	31
23.	EBT Test Data Augmentation Factor's Versus Mach Number .....	32
24.	Effect of Integral Scale on Augmentation Factors.....	33
25.	Effect of Integral on Correlation of Augmentation Factors to $\lambda$ .....	33
26.	Linear Curve Fit of $(r/r_o)^{2.69}$ versus $\lambda$ .....	36
27.	Ratio of Blowing to Non-Blowing $\lambda$ Versus Shear Mach Number .....	38
28.	Correlation of $\lambda$ Function to Shear Mach Number .....	39
29.	Augmentation Factor Versus Mach Number ( $r_o/r_o\text{-ref}=1.072$ , $D_o/D_o\text{-ref} =1.0$ , PBAN Binder) .....	41
30.	Augmentation Factor Versus Mach Number ( $r_o/r_o\text{-ref}=0.830$ , $D_o/D_o\text{-ref} =1.0$ , HTPB Binder) .....	41
31.	Augmentation Factor Versus Mach Number ( $r_o/r_o\text{-ref}=1.20$ , $D_o/D_o\text{-ref} =1.0$ , PBAN Binder) .....	42
32.	Augmentation Factor Versus Mach Number ( $r_o/r_o\text{-ref}=6.05$ , $D_o/D_o\text{-ref} =0.333$ , HTPB Binder) .....	43
33.	Interior Ballistics Analysis Results for Motor 6 .....	43

## LIST OF TABLES

<u>Table</u>	<u>Title</u>	<u>Page</u>
1.	Heats of Formation of Considered Species.....	10
2.	Finite Rate Model Results.....	13
3.	Normalized Characteristics of the Test Motors.....	37

## I. INTRODUCTION

Interior ballistics of solid propellant rocket motors continues to be an engineering discipline that is conducted primarily on the macro scale. Although considerable advancements in micro scale ballistics modeling are being made, such as the work conducted by the Georgia Institute of Technology's Computational Combustion Laboratory (CCL) and the University of Illinois-Champaign Urbana's Center for Simulation of Advanced Rockets (CSAR), micro scale modeling remains relatively impractical, in terms of computational time and resources, for design phase changes and general performance analysis. In fact, the performance of most rocket motor designs can be predicted very accurately using macro scale models that rely on accurate burning rate, surface history, and propellant thermochemistry. This is particularly true beyond the ignition transient when most motors operate in a quasi-steady condition in that the motor pressure changes as the surface area and throat area changes on a time scale that can be orders of magnitude greater than the time scale of near-wall effects such as the chemical kinetics of the combustion process or the lifetime of turbulent flow features below the Kolmogorov scale.

Prior to settling into quasi-steady operation, some rocket motor designs contain pressure spike features which must be adequately captured with macro scale models such that overall system impact can be assessed, but also because these spikes may alter the surface regression pattern and impact the quasi-steady performance analysis. Pressure spikes can be attributed to igniter discharge, transient propellant burning, and erosive burning. Of these three, erosive burning is typically most significant because the duration of the event is longer and because the surface regression can be significantly altered. For the macro scale ballisticians, prediction of erosive burning can be an arduous task given that erosive burning represents an increase in the rate of pyrolysis of the solid phase of the propellant and the combustion process that is in general complete within a few hundred microns from the propellant surface. Several macro scale erosive burning models have been available since the early 1950's, and use macro scale independent variables, such as bore diameter, Mach number, and mass flux, to calculate a burning rate augmentation that is induced from the cross-flow. Most of these models contain several constants of proportionality which must be calibrated to test data and also lack a universal scaling law making the models ineffective as a predictive tool.

Presented in this report are the results of an effort to develop a macro scale universal erosive burning scaling law and model. The development of the model begins with considerable micro scale combustion modeling of solid propellant in cross-flow. Various wall shear stress flow conditions are imposed on sundry propellant burn rates or mass injection rates. A universal scale law is proposed which is based on what is termed the "wall momentum ratio," or the ratio of the cross-flow momentum to the injection momentum. From this proposed law, a macro scale erosive burning model is presented along with application results. The objective of this approach is to incorporate micro scale physics into macro scale models such that the interior ballisticians can better predict erosive burning. The micro scale modeling is based on a two-flame, finite-rate chemistry model of the solid propellant combustion process which appears to be adequate to meet the objectives of this work. Other studies are being conducted [1] that incorporate a three flame model which may prove useful in improving the accuracy of the present proposed model or develop a replacement. Details of the work herein can be found in two limited distribution papers and one open source paper published between 2005 and 2009 [2, 3, 13].

## II. BACKGROUND

Erosive burning is a term used in the solid rocket motor community to describe the phenomenon of the increased pyrolysis rate (burn rate) of a solid propellant that is directly attributed to tangential gas flow along the surface [4]. Analogous to simple convective heat transfer, as the tangential velocity of the hot gas is increased, the heat flux into the propellant surface is increased. The additional energy flux at the surface boundary must be balanced by an increase in either conduction into the solid, or an increase in the pyrolysis rate at the surface. Characterization of the burning rate of a solid propellant is critical in the design process of a rocket motor in that the exposed surface area, throat area, burn rate, and other design parameters must be jointly selected such that the resulting performance, and specifically the internal gas pressure, can be predicted and accommodated by the supporting structure.

For simplicity, propellant burn rate data is typically collected in environments that approximate quiescence, such as a stand burner test fixture (Fig. 1).

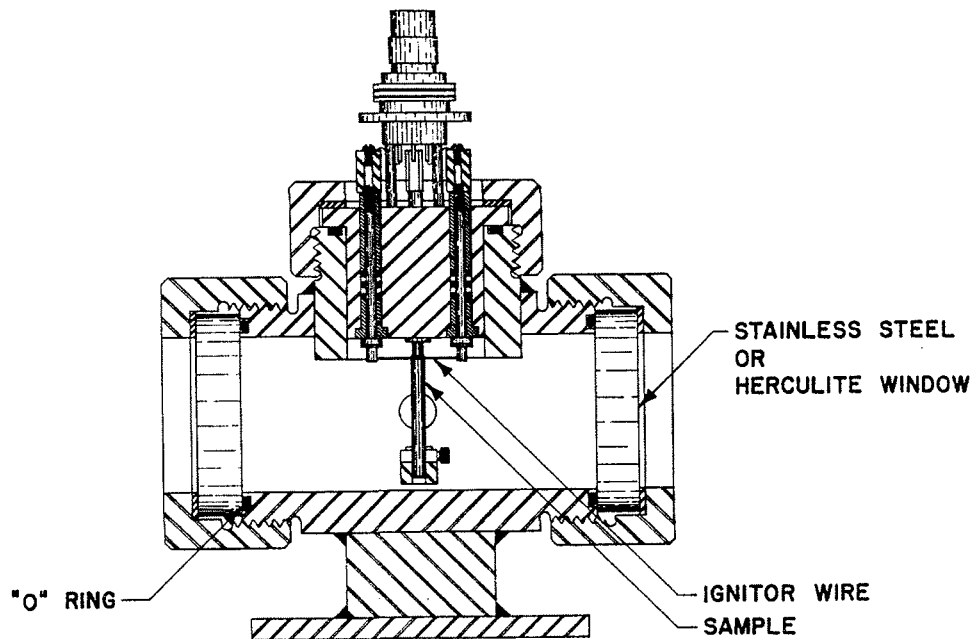


Figure 1. Window Bomb Strand Burner

In such an environment, the propellant's burning rate is predominately a function of the pressure of the environment and the initial temperature of the solid propellant. Holding the initial temperature of the solid constant, the burning rate is characterized over a range of pressures, and normally correlates to pressure with a function of the form  $r=aP^n$ . Data collected in such a fashion is usually referred to as the propellants base burning rate ( $r_o$ ).

When a given propellant is removed from the quiescent environment, the demonstrated burn rate may exceed the base rate measured at the same environmental pressure. This increased rate is termed erosive burning, and is often quoted as a ratio of the demonstrated rate to the base rate as  $r/r_o$  (augmentation factor). Substantial historical data shows that the magnitude of this ratio is a function of the tangential velocity of the gas flowing over the surface of the propellant, and the magnitude of the base rate itself [5]. Clearly, the dependence on the cross-flow velocity can be seen as increased convection-driven heat transfer at the surface, but the base rate dependency is not as straightforward. Erosive burning will manifest itself with a characteristic spike or “hump” in the head-end pressure at the beginning of the trace. Excessive erosive burning will often cause the pressure tail-off during blow-down to occur at a shallower angle as a result of propellant slivers forming along the length of the regressing grain. Figure 2 shows a comparison of test data collected on a motor with erosive burning evidenced in the trace to a simulation of the motor where no erosive burning is considered.

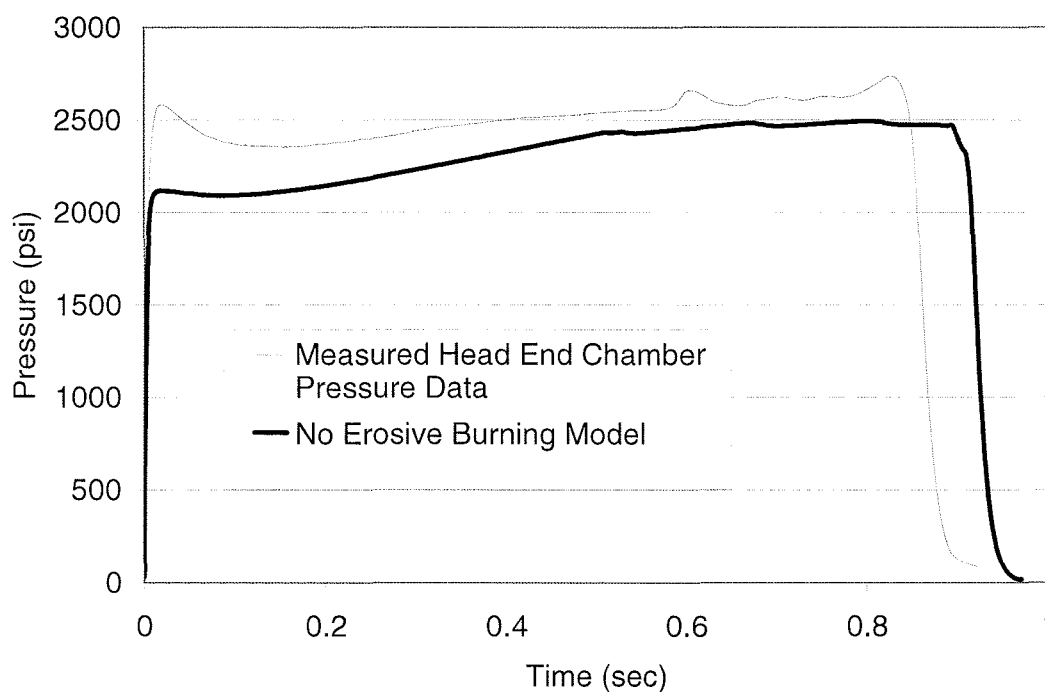


Figure 2. Measured Chamber Pressure

Further examination of erosive burning test data shows that as the cross-flow velocity over a burning propellant is gradually increased (holding the environment pressure constant), there is initially little to no increase in the demonstrated burning rate. However, at some magnitude of velocity, the demonstrated burning rate takes on a clear dependency on the cross-flow velocity. The point at which this dependency on velocity begins is called the threshold velocity. Or, more typically, the cross-flow conditions are described in terms of Mach Number, and thus the threshold point is termed the threshold Mach Number.

Most erosive burning models are empirically derived from full-scale motor data. Several correlations have been developed that attempt to capture the dependencies demonstrated in the test data. The form of most models generally contain some function of the bulk Mach Number in the motor or test fixture. The popularity of the use of Mach Number is most likely due to the extended use of One-Dimensional (1-D) interior ballistics codes that cannot directly utilize correlations based on near-wall information. Admittedly, holding all other variables constant (hydraulic diameter, pressure, and base rate), excellent correlations of the augmentation factor to Mach Number can be demonstrated, with the resulting function approaching linearity as the Mach Number increases beyond the threshold value. However, Mach Number, within itself, gives no physical insight into the controlling mechanism, and most specifically, gives no insight into the threshold point.

Assuming that increased heat transfer due to increased velocity is the fundamental controlling mechanism in the erosive burning problem, more physical insight should be obtained through the use of correlation variables that are typical to convection heat transfer problems, such as  $Re$ ,  $Pr$ ,  $D_{hyd}$ , and  $\mu$ . Recent Computational Fluid Dynamics (CFD) based numerical research has approached the erosive burning problem from a more physical perspective by attempting to correlate the erosive burning augmentation factor to wall shear stress ( $\tau_{wall} = \mu dU/dy$ ) by logic of the Reynolds Analogy. Wang, et al. [6] have developed an erosive burning model using a power law function of wall shear stress. Using a sophisticated test fixture that allows for the measurement of the local surface regression rate via ultrasonic's, the demonstrated burn rate is correlated to shear stress by combining the test results with a Reynolds-Averaged, Navier-Stokes (RANS) CFD model of the test fixture gas dynamics. The local calculated wall shear stress is then paired with the local measured burn rate producing a power law function of the form

$$r/r_{base} = c_1 + c_2 (\partial u / \partial y)^{c_3} \quad (1)$$

The resulting correlation has been successfully used to predict the chamber pressure of rocket motor designs that are scaled up from the test article. Another variation of the use of wall shear stress in erosive burning correlations is reported by Bulgakov, et al. [7, 8] where test data is plotted versus a ratio of a skin friction function and the mass injection ratio.

The erosive burning threshold problem has been studied by Godon, et. Al. [9] using the Spalding-Pantankar method. The numerical study is developed around the idea that erosive burning is due to the penetration of turbulence into the flame zone. The results of the study are presented as a function of the specific mass flow rate, and utilize two Reynolds numbers based on the axial flow velocity and the injected mass velocity. A conclusion of the work is that the threshold condition is strongly dependent on the motor geometry size.

Razdan and Kuo [10] have compiled an extensive summary of erosive burning modeling and erosive burning correlations. These correlations extend back to the 1940's beginning with the Lenoir-Robillard equation [11]. In most attempts to develop a predictive erosive burning model, mass flux, both axially and injected, is used in some form. Most recently, Mukunda and Paul [12] have studied the universal behavior of erosive burning, and concluded that the erosive burning effects are contained in two parameters ( $\eta$ ,  $g$ ) where  $\eta$  is a function of the augmentation factor, and  $g$  is a function of the mass flux and the Reynolds number based on mass flux ( $Re_o$ ).

Highly resolved combustion and flow-field modeling has been used to study the erosive burning problem with success [13]. The near-wall region of a burning solid propellant is modeled at the Kolmogorov scale using a 2-step finite rate chemistry model. For a fixed geometry, the augmentation factors as a function of Mach Number were calculated, with the resulting function used in the headend pressure prediction of a full-scale motor. The results matched test data very well, and confirmed that erosive burning is a near-wall phenomenon.

An observable trend in erosive burning data is that the augmentation factor at a given bulk velocity or Mach Number value changes as the base burning rate of the propellant changes. In general, the augmentation factor varies inversely to the base rate at a constant bulk velocity. The threshold velocity appears to shift as well, to the extent that if the geometry of the motor is fixed, the base rate can be increased such that no erosive burning is observed at any bulk Mach Number value. Physically, as the burning rate increases, a mass balance at the propellant surface dictates that the gas injection velocity normal to the surface, and thus perpendicular to the cross flows, will increase. The relationship between the burning rate and the injection velocity is demonstrated through a conservation of mass at the propellant surface as

$$\Gamma \rho_p = v_{inj} \rho_g \quad (2)$$

In terms of momentum, as the injection velocity increases, the ratio of the cross-flow momentum and injection momentum decreases ( $\rho u^2 / \rho v^2$ ).

When viewed from the perspective of cross-flow to injection momentum ratio, a physical explanation of the threshold velocity, and the base rate dependency of the augmentation factor can be postulated. Within a certain regime of momentum ratio, the heat transfer, temperature gradient, and other variables, are dominated by the injection momentum. The cross-flow momentum is insufficient to disrupt the near-wall conditions, and thus the heat transfer to the surface appears to match that which would be seen in the quiescent environment. Thus, the augmentation factor is near zero, and erosive burning is not present. As the cross-flow momentum increases, or the injection momentum decrease, the near-wall conditions become influenced and ultimately dominated by the cross-flow and then the augmentation factor varies with a strong dependency on the cross-flow variables (wall shear stress, bulk Mach Number).

The purpose of this report is to present a numerical study of the near-wall region of a burning solid propellant correlating the results to a nondimensional quantity termed the wall momentum ratio. In addition, the presented numerical results will demonstrate the erosive burning threshold condition and offer physical insight into the phenomenon. Using near-wall modeling, the regression rate of a sample solid propellant is calculated over a range of cross-flow

velocities and base burning rates (injection velocities). A two-step global finite rate chemistry model is used to establish the locations of the two primary flames in composite solid propellants. The condensed or solid phase of the propellant is resolved equally to the gas phase, such that the temperature gradient at the surface of the propellant can be adequately addressed. Grid spacing is below the Kolmogorov turbulent scale such that near-wall turbulent structures can be directly resolved. In each analysis group, a quiescent calculation is made to establish the base burning rate for the selected thermodynamic properties. Holding the thermodynamic properties constant, additional calculations of burning rate are made for a range of cross-flow velocities. The resulting augmentation factors are correlated to the cross-flow-to-injection momentum ratio. The procedure is repeated for a new set of thermodynamic variables, and thus a new base rate. Using the results of the highly resolved, near-wall modeling and the wall momentum scaling law, a macro model will be developed for the incorporation into interior ballistics codes.

### III. MODEL DESCRIPTION

#### A. Overview of Numerical Simulation Code

Resolution of the flow field below the Kolmogorov scale eliminates the need for subscale models. The flow structures are resolved directly by a time-accurate integration of the conservation equations. A fully compressible, Two-Dimensional (2-D), finite differencing code has been written based on an extended MacCormack scheme [14]. The advantage of this approach is the simplicity in implementation, and second order accuracy in time and approximately fourth order accuracy in space. Nonuniform grid spacing or grid stretching is used to concentrate the mesh in regions of large gradients, which primarily occur at the burning surface. Grid stretching also aids in the suppression of numerical induced oscillations. Characteristic boundary conditions are applied at the inlets and outlets. Conduction in the solid propellant is resolved with a second order, central scheme. Surface or boundary gradients are resolved with second or third order forward or backward schemes.

#### B. Governing Equations

The governing equations that are solved in the analysis of the erosive burning problem are the conservation of mass, momentum, and energy, as well as the ideal gas equation of state. In addition, a finite rate chemistry model is used along with the conservation of species and the caloric equation of state. The conservation equations are listed below in order of the conservation of mass, momentum, energy ( $E$ =Total Energy,  $q$ =Heat Flux), the ideal gas equation of state ( $R_u$ =Universal Gas Constant), the conservation of species, and the caloric equation of state:

$$\left\{ \begin{array}{l}
\partial_i \rho + \partial_i (\rho u_i) = 0 \\
\partial_i (\rho u_i) + \partial_j (\rho u_i u_j) = -\partial_j p \delta_{ij} + \partial_j \tau_{ji} \\
\partial_i (\rho E) + \partial_i (\rho u_i E) = -\partial_i q_i - \partial_i (\rho u_i) + \partial_j (\tau_{ji} u_i) \\
p = \rho \frac{R_u}{MW} T \\
\partial_i (\rho Y_m) + \partial_i [\rho Y_m u_i + \rho V_{i,m} Y_m] = \dot{\omega}_m, \quad m = 1, N \\
h_m = \Delta h_{f,m}^o + \int_{T_o}^T c_{p,m}(T) dT
\end{array} \right. \quad (3)$$

For a given propellant formulation and selected applied pressure, thermochemical equilibrium calculations (NASA-Lewis Code) [15] are made to find the viscosity ( $\mu$ ) and the Prandtl Number ( $Pr$ ). The conductivity is then calculated as  $k_g = \mu C_p / Pr$ , where the gas specific heat ( $C_p$ ) and Molecular Weights ( $MW$ ) are also derived from the equilibrium calculations.

### C. Gas Phase Boundary Conditions

The computational domain consists of a 2-D channel with the burning propellant located on the bottom wall. Following the work of Poinot and Lele [16], characteristic boundary *conditions* are prescribed at the domain's inlet and outlet. The solid bottom wall is treated as a no-slip surface, and the inlet and outlet are treated as non-reflecting, subsonic boundaries. The gas entering the domain by cross-flow is assumed to be combustion products with a stagnation temperature equal to the adiabatic flame temperature of the propellant. At the solid propellant surface, solid propellant decomposition products enter the domain at the decomposition temperature. An Arrhenius expression of the following form [17, 18] is used to relate the surface regression rate to the surface temperature.

$$r = cP^n \exp \left[ \frac{E_a}{R_u} \left( \frac{1}{T_{surf,o}} - \frac{1}{T_{surf}} \right) \right] \quad (4)$$

The inlet temperature profile assumes a constant total temperature equal to the adiabatic flame *temperature* of the solid propellant combustion products. The inlet velocity boundary condition assumes a turbulent profile that is developed out to the extent of the computational boundary.

The outlet characteristic boundary condition is set as a non-reflecting subsonic outlet. This condition assumes constant pressure at infinity, with the pressure at the outlet adjusted by characteristic waves that are assumed to propagate from the constant pressure reservoir at infinity. Thus, the specified computational pressure sets the pressure of the far-field reservoir, but does not rigidly fix the exit pressure, but allows it to relax to the far-field condition. Following the work of Sutherland, et. Al. [19], chemical reaction source terms are retained in the characteristic boundary condition equations.

## D. Thermal Transport Model

Fundamentally, the pyrolysis rate of the solid propellant is determined by the surplus energy flux into the surface. The convected or radiated energy from the gas to the surface must be balanced by either conduction into the solid or pyrolysis of the surface. Therefore, a thermal transport model which accurately establishes the temperature gradient at the surface, and thus the conduction into the solid, must be used. The energy equation for the solid reduces to  $\rho_p C_s \partial_t T = \partial_i (k_s \partial_i T)$ . The conductivity ( $k_s$ ), specific heat ( $C_s$ ), and density ( $\rho_p$ ) of the solid propellant are assumed to be spatially invariant (solid phase is assumed to be homogeneous)<sup>1</sup>.

Because the solid propellant boundary is a pyrolyzing or moving surface into the cold propellant, the temperature gradient at the surface in the solid will be influenced by the rate at which the surface moves. A moving grid could be used to account for the regressing surface, but in the context of this analysis is not preferable given the local wall irregularities that would be generated. To account for the regressing surface without moving the grid, the thermal transport equations are adjusted to account for a moving reference frame, based on the local burn rate. The propellant is assumed to be fed into the combustion chamber at the rate the propellant is burning. The bottom of the propellant is held at ambient temperature sufficiently far from the surface such that heat will not penetrate the full depth during the analysis time. The conduction equation in the normal direction is modified such that the rate of conduction is reduced by the rate cold propellant is fed up to the surface. The resulting equation is of the form

$$\frac{\partial T}{\partial t} = \alpha \left( \frac{\partial^2 T}{\partial y^2} + \frac{\partial^2 T}{\partial x^2} \right) - r \left( \frac{\partial T}{\partial y} \right) \quad (5)$$

where the energy deficit is carried to the surface by way of the burning rate and the local temperature gradient.

## E. Gas-Solid Interface

The emissivity of the gas is primarily a function of the gas pressure and composition; thus, the radiation flux is assumed to be invariant with cross-flow, provided the pressure remains reasonably constant. As such, radiation is ignored in this analysis. The surface energy balance equation is then of the form  $q_{gcon} = q_{pcon} - Q\mathbf{M}$ , or in expanded form  $k_g \partial_i T = k_s \partial_i T - Q\mathbf{M}$ .  $\mathbf{M}$  is the mass flux from the burning propellant and can be related to the burn rate or pyrolysis rate as  $\rho_p r$ . The velocity of the gas injected from the burning propellant is calculated from a mass balance at the surface as  $\rho_p r = \rho v_{norm}$ , where  $v_{norm}$  is the gas velocity normal to the propellant surface.

---

<sup>1</sup> Propellant homogeneity is not a restriction in this numerical approach, but a simplifying assumption. The author has demonstrated the numerical approach for a nonhomogeneous surface with discrete AP and binder locations.

## F. Finite Rate Chemistry Model

Two distinct heat release regions or flames are treated in this analysis<sup>2</sup>. The heat feedback, and thus position, from these flames and from the free stream to the propellant surface determines the rate at which the propellant will pyrolyze. The two flames are AP decomposition, and the decomposed AP and binder reaction.

All species are assumed to have the same mass diffusivities found from the Lewis Number ( $Le = \alpha/D$ , where  $\alpha$  is the thermal diffusivity and  $D$  is the mass diffusivity). The four chemical species considered in the analysis are AP gas, APd gas, binder gas, and combustion products. Two chemical equations, shown in Equation (6), are required to relate these species in the chemical model:



where  $\beta$  is the mass stoichiometric coefficient. Two global reaction rate equations are required to complete the chemical model and are shown in Equation (7)

$$\begin{aligned} R_1 &= D_1 P_o^{n_1} [AP] \exp\left\{-\frac{E_1}{R_u T}\right\} \\ R_2 &= D_2 P_o^{n_2} [APd][Binder_{Gas}] \exp\left\{-\frac{E_2}{R_u T}\right\} \end{aligned} \quad (7)$$

where the [ ] quantities are the concentrations of the species, and  $D_i$ ,  $n_i$ , and  $E_i$  have been taken from previous studies and represent experimental data [17]. The law of mass action is used to complete the rate of production of the remaining two species. The finite rate chemistry model input is  $D_1 = 2.234 \times 10^7$ ,  $D_2 = 1.105 \times 10^7$ ,  $E_1/R_u = 8000$  K,  $E_2/R_u = 11000$  K,  $n_1 = n_2 = 1.0$ , and  $\beta = 8.1$  (units for  $D$ 's are for  $P = atm$ , and [ ] =  $kmol/m^3$ ).

## G. Model Definition and Boundary Conditions

The mass fractions of all species are set at the boundaries, as well as initially throughout the computational domain. Heats-of-formation ( $h_f^0$ ) for all species are specified such that the split of chemical energy to sensible energy may be tracked. Species diffusion velocities are calculated, and thus require the input of mass diffusivities.

---

<sup>2</sup> Unless the Aluminum particle size is on the sub-micron level, the Aluminum flame can be assumed to occur in the far field region.

The total heat release from all reactions is set equal to the adiabatic heat release of the propellant as calculated by thermochemical equilibrium. Since only two reactions are considered, the heat release from the APd flame and the APd-HTPB flame must sum to the total heat release from the propellant. For an adiabatic system, the total enthalpy of a reaction is constant, only the distribution between sensible ( $h_s$ ) and chemical enthalpy changes as shown in Equation (8)

$$\begin{aligned} (h_f^o + h_s)_{AP} &= (h_f^o + h_s)_{APd} \\ \eta(h_f^o + h_s)_{APd} + (1 - \eta)(h_f^o + h_s)_{HTPB} &= (h_f^o + h_s)_{Products} \end{aligned} \quad (8)$$

where  $\eta$  represents the mass fraction of the APd in the APd-HTPB reaction. A thermochemical equilibrium calculation is run to find the adiabatic heat release, or sensible enthalpy of the APd reaction. From this, and the heat of formation of the AP, the heat of formation of the APd is calculated. The heat of formation of the final combustion products is then found from Equation (8) by setting  $h_s$  of the products to the thermochemical calculation value, and  $h_s$  of the HTPB to the tabulated value. Table 1 shows calculated values for a typical composite propellant.

Table 1. Heats of Formation of Considered Species

Ammonium Perchlorate - $h_f^o$	-2520.51 kJ/kg
Ammonium Perchlorate	-5205.2 kJ/kg
Decomposed - $h_f^o$	
HTPB - $h_f^o$	-1001.5 kJ/kg
Combustion Products - $h_f^o$	-9820.1 kJ/kg

#### IV. DEVELOPMENT OF THE WALL MOMENTUM FUNCTION

##### A. General Discussion and Test Data

Erosive burning modeling is generally conducted as a submodel of a larger rocket motor performance simulation or prediction analysis. Thus, the measure of the model’s validity is usually restricted to an assessment of the predicted motor headend pressure as compared to test data in a ballistics analysis which utilizes the erosive burning correlation in question. Some scaling information may be gained from this approach, but little physical insight into the controlling mechanisms is acquired. Ultrasound burn rate measurement techniques have made possible the collection of local surface regression rates within a combustion chamber at local flow conditions, and thus offer an opportunity to validate erosive burning models based on a measured local surface regression rates as opposed to a global quantity, such as headend pressure.

Furfaro constructed a 5-inch Center Perforated Propellant Grain (CP), segmented motor for the purpose of gathering ultrasound surface regression information for various propellants, base burn rates, pressures, etc. [20] The actual measured surface regression rate is normalized by the propellants base burning rate ( $r = aP^n$ ) at the local pressure conditions. Some of this data is plotted in Figure 3 which shows an augmentation factor ( $r/r_o$ ) versus Mach number. The Mach number presented represents the numerically derived (1-D flow calculations) local bulk Mach number.

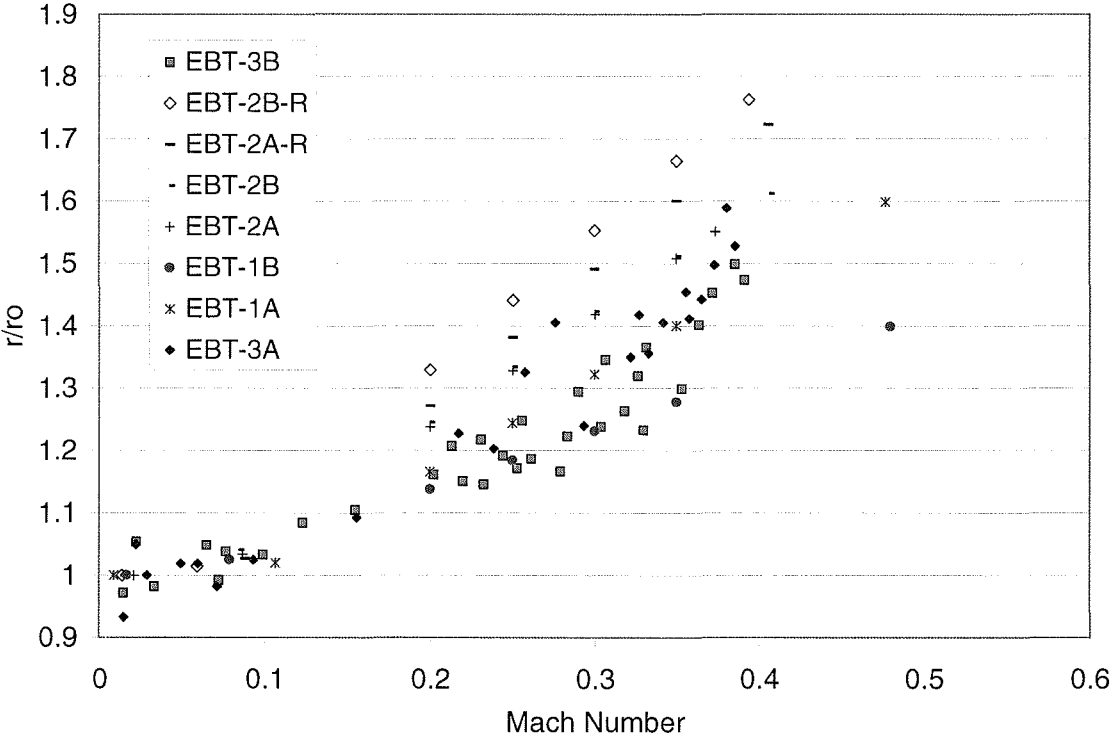


Figure 3. 5-Inch CP Augmentation Factor Data

The data presented is taken over a period of time where the local pressure is changing which means the local base burn rate is changing as well. The data points do not represent an instantaneous  $r/r_o$ , but are normalized by calculating an average  $r_o$  at the average local pressure during the test duration. Clearly shown in the data is a slope change in the augmentation factors between a Mach Number of  $M=.05$ , and  $M=0.1$ . In fact, a linear curve fit of the data up through approximately  $M=0.08$  produces a slope that is near zero. The Mach number at which the data departs from a near zero slope is considered to be the threshold Mach number for erosive burning. The originators of this data state  $M=0.08$  as the threshold Mach Number for this data set.

### B. Numerical Modeling of a High Burn Rate-High Shear Geometry

The numerical modeling and analysis technique is first tested on a solid rocket motor geometry that has a base burn rate in excess of 2 in/sec at 1000 psi, and Mach numbers that reach 1.0 at the aft end at ignition. Typically, motors with high burning rate propellants do not exhibit erosive burning; however, as Figure 2 shows (Fig. 2 shows test data for the present geometry) considerable evidence of erosive burning is evident during the initial portion of the motor burn. As will be discussed later, the excessive cross-flow shear is believed to induce the witnessed erosive burning in spite of the high burn rate.

A base case is run to establish the thermodynamic parameters that produce the desired base burning rate in an environment with no cross-flow (calibration of the model to the base burn rate of the propellant in question). Additional runs are conducted in cross-flow conditions ranging in bulk Mach Numbers from  $M=0.0$  to  $M=0.8$ . Each solution is run until a statistically steady condition is reached, producing a calculated propellant regression rate for the given flow conditions. Figure 4 shows a schematic of a typical computational domain.

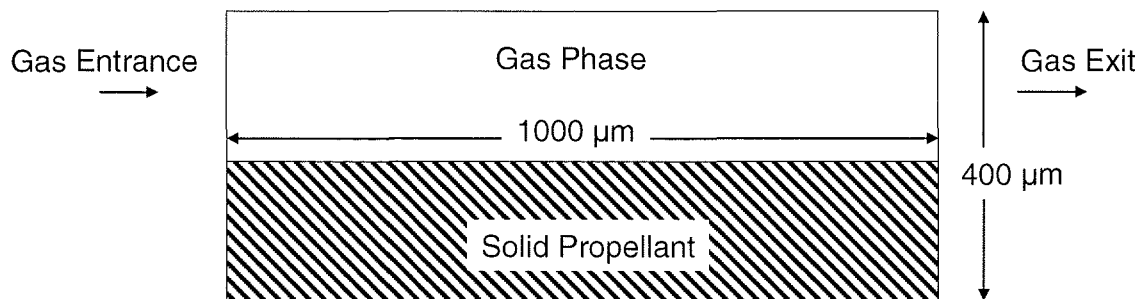


Figure 4. Schematic of Computational Domain

Table 2 shows the results from the series of near-wall calculations. The Mach Number is calculated from the assumed integral scale of the test article and the bulk axial velocity. The burn rate at  $M=0.0$  reflects the desired base rate of the propellant. The rate ratio shows the calculated augmentation rate that results from the cross-flow.

Table 2. Finite Rate Model Results

Mach Number	Rate (cm/s)	Surface Temperature (K)	Rate Ratio ( $r/r_0$ )
0.0	5.295	1143.80	1.000
0.1	5.444	1147.02	1.028
0.5	6.018	1158.89	1.137
0.8	6.453	1167.22	1.219

The calibration run for  $M=0.0$  results in a surface temperature of  $1143.8\text{ K}$ . The normalized rate increase ranges from  $2.8\text{ percent}$  at  $M=0.1$ , up to  $22\text{ percent}$  at a free stream  $M$  of  $M=0.8$ . The normalized surface temperature increases associated with the predicted rates range from  $.28\text{ percent}$  at  $M=0.1$  up to  $2.0\text{ percent}$  at  $M=0.8$ . The results show that the surface temperature increase is small compared to the rate increase, due to the high activation energy in the pyrolysis law.

Figure 5 shows a comparison of the near-wall temperature gradients in the normal direction at the mid-point of the burning propellant.

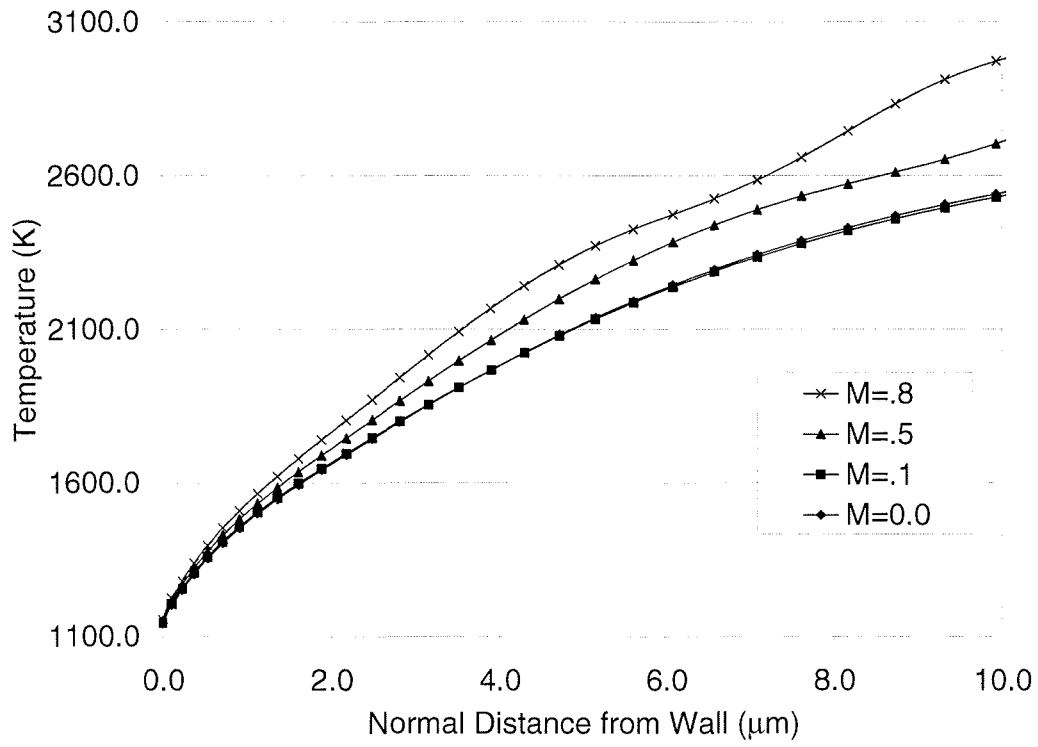


Figure 5. Near-Wall Temperature Profile

The gradients are as expected, showing an increase near the wall as the free-stream  $M$  increases. Figure 6 shows these gradients out to the extent of the thermal boundary layers. The increase in heat transfer to the wall as the  $M$  increases is evident in the curves. The curve for  $M=0.8$  shows considerable deviation from the isentropic and adiabatic entrance profile.

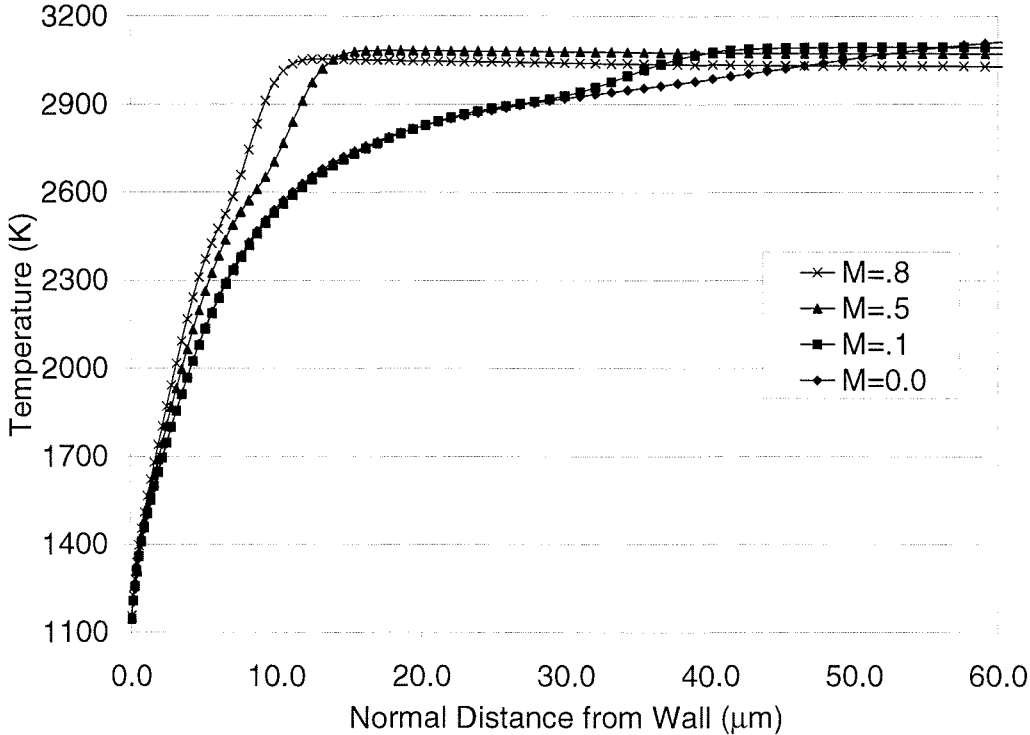


Figure 6. Temperature Profiles Out to Thermal Boundary Layer Edge

The flame thicknesses for the AP decomposition flame and the APd-Binder flame are shown in Figure 7 for the  $M=0.0$  calibration analysis.

Figure 7 shows a very thin decomposition flame which approaches the resolution limits of the model. However, several grid points exist between the wall and the maximum reaction rate region. The flame is on the order of 3 microns thick. The APd-binder premixed flame is highly resolved and approaches 40 microns in thickness.

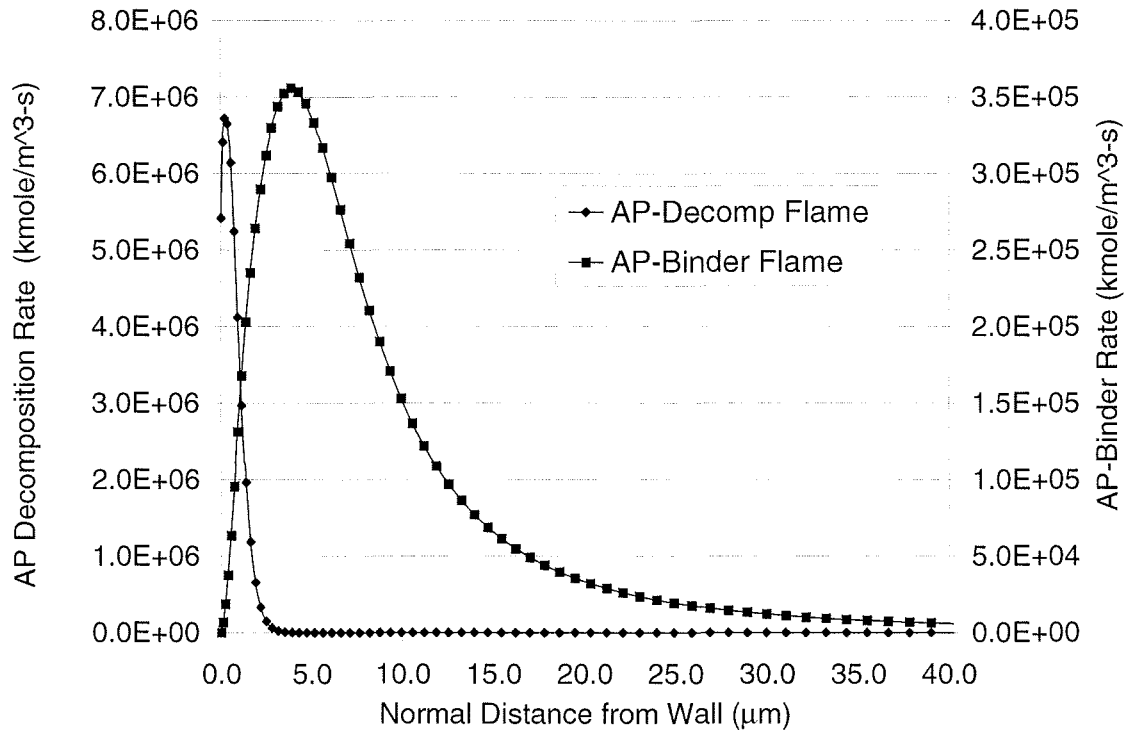


Figure 7. Comparison of the AP Decomposition and APd-Binder Flame Thicknesses for  $M=0.0$

Figures 8 and 9 show the effect of increasing the cross-flow velocity on the flame thicknesses. Of great interest is that as the  $M$  increases, the flame thicknesses decrease, but the relative distance of the maximum reaction rate from the wall changes very little. Of note in Figure 9 is that the increase in  $M$  has only a slight effect on the AP decomposition flame thickness. This slight thickness decrease is attributed to the increase in temperature, due to the compressed boundary layer, that produces a reaction rate increase near the wall.

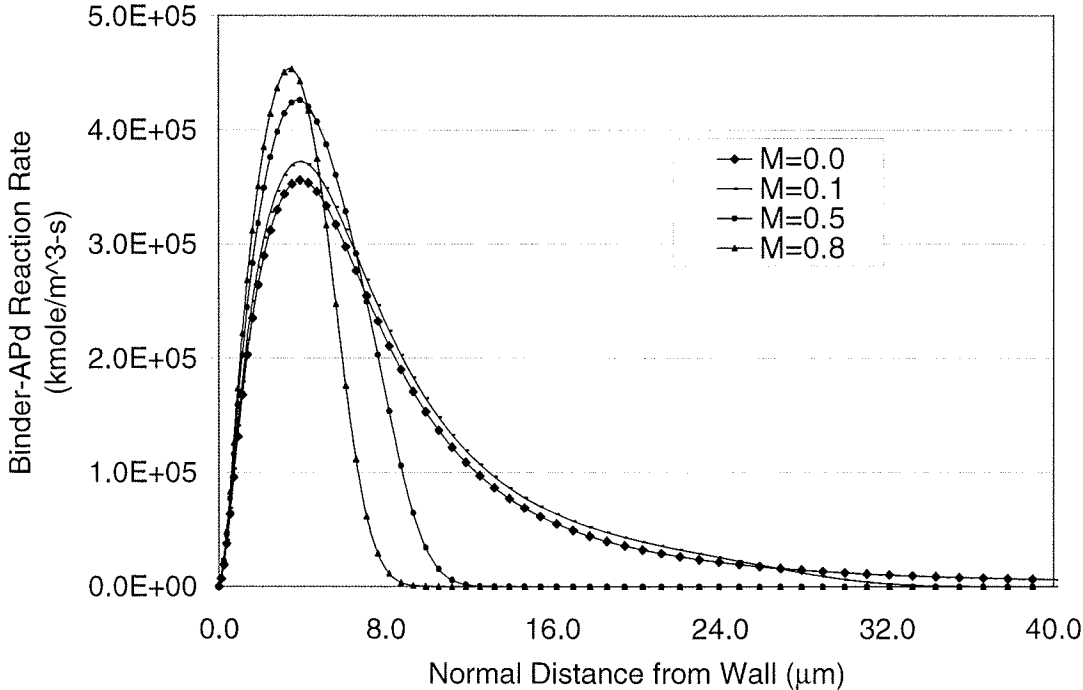


Figure 8. APd-Binder Flame Thickness Comparison for Various Free-Stream Mach Numbers

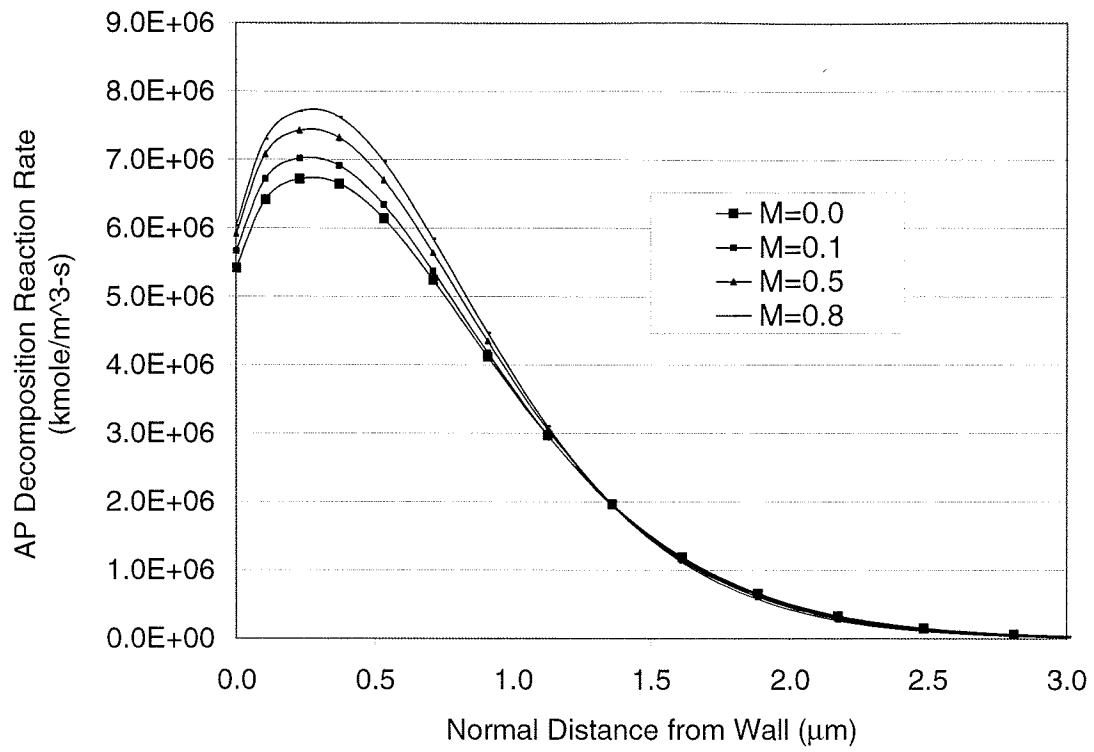


Figure 9. AP Decomposition Flame Thickness Comparison for Various Free-Stream Mach Numbers

Figure 10 shows that as the  $M$  increases, the near-wall vorticity increases, with the maximum point moving close to the outer edge of the diffusion flame.

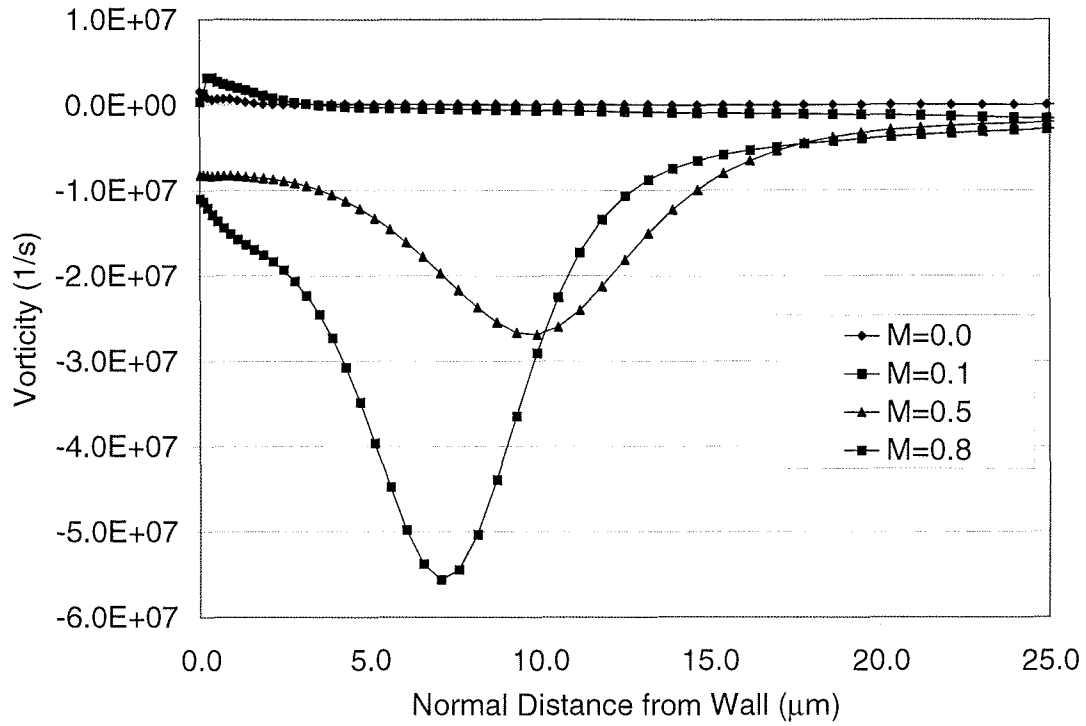


Figure 10. Near-Wall Vorticity for Various Free-Stream Mach Numbers

This is shown more clearly in Figure 11, where the APd-Binder flame is plotted with the vorticity for a free-stream  $M$  of  $M=0.8$ .

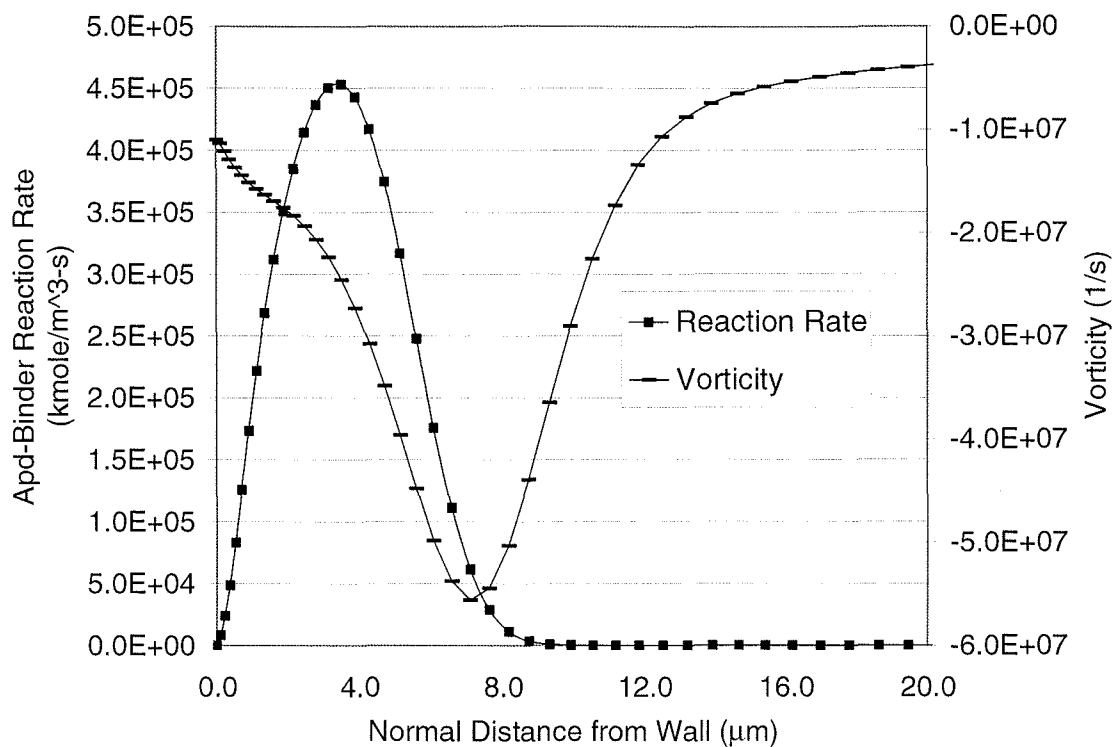


Figure 11. APd-Binder Flame and Vorticity for  $M=0.8$

The source of the vorticity is shown in Figure 12 where the tangential velocity profiles are plotted. The plot shows considerable lifting of the velocity boundary layer due to the side injection of the combustion gases, thus creating large tangential velocity gradients in the normal direction.

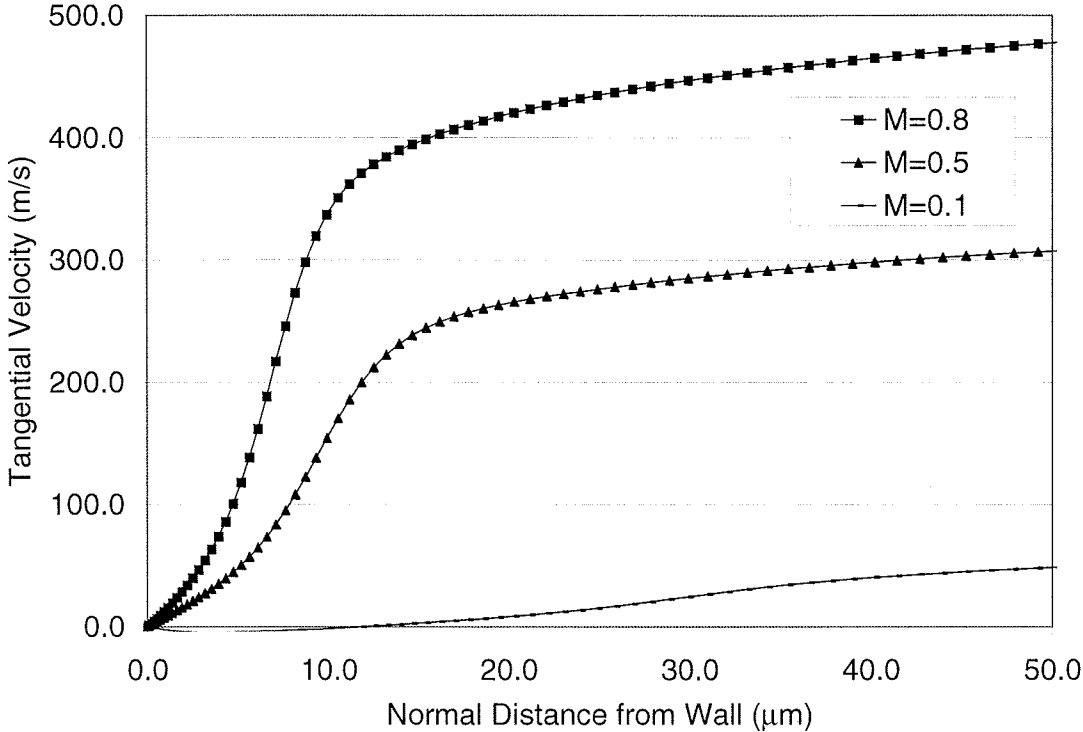


Figure 12. Near-Wall Tangential Velocity Profiles

The net result appears to be an increase in the reaction rate of the decomposed AP and binder gases, with a resulting decrease in the flame thickness. The stand-off distance of the point of maximum heat release of the decomposition flame changes little.

The starting location of the premixed flame is dependent on the pre-cursor AP decomposition flame. Since there is little change in the decomposition flame, the start of the APd and binder flame remains relatively stationary. Thus, the results show that turbulence reduces the APd and binder flame thickness, but does not significantly change the stand-off distance of the location of the maximum heat release zone.

Figure 13 shows that the thermal gradient is fairly constant from the edge of the thermal boundary down to the wall. No discontinuities are shown in the thermal profile as it passes through the APd and binder flame.

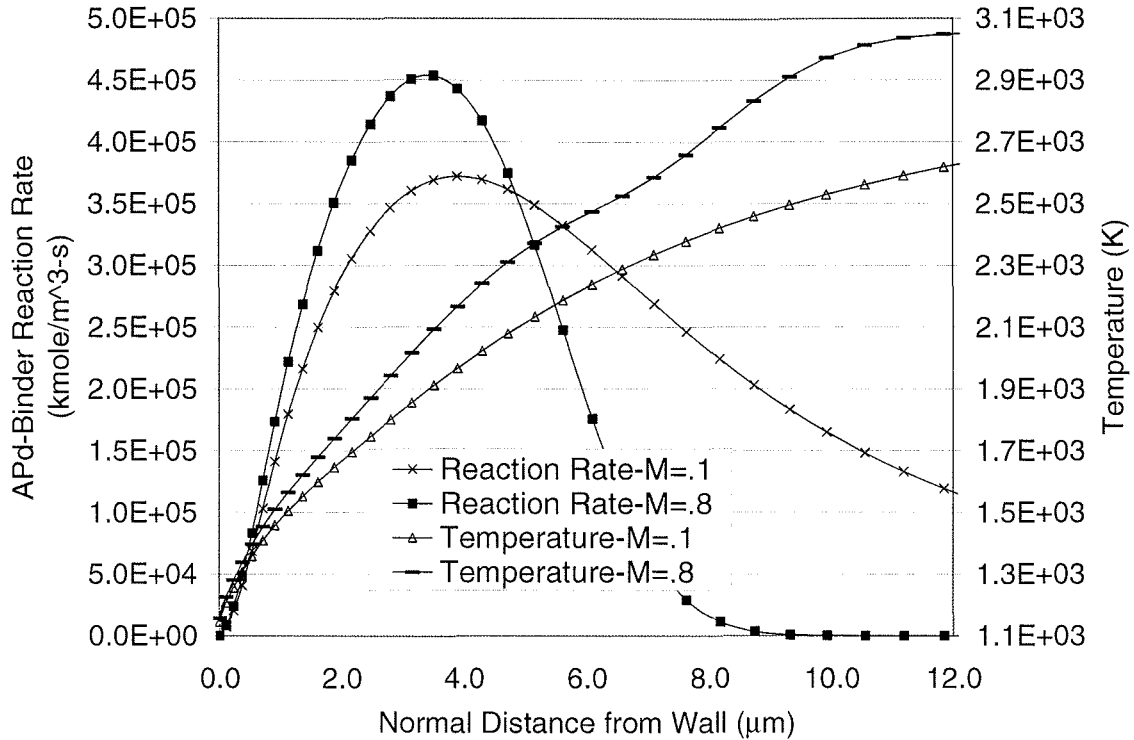


Figure 13. Comparison of Reaction Rate Gradients to Thermal Gradients

Since the regression rate is determined by the energy balance at the solid gas interface, the conclusion is that the controlling parameters in the heat flux to the surface are the surface temperature and the free stream conditions. Although the temperature gradient at the wall varies with  $M$ , it appears to be weakly influenced by the flame zone.

Figure 14 shows a comparison of how the thermal gradient develops at the gas-solid interface for both a high and low burn rate propellant at the same cross-flow conditions. On the gas side, the slopes converge from approximately 5 microns down to the wall. The solid side shows a distinct difference in slope. The low rate propellant allows the surface heat to penetrate further into the solid resulting in a shallower slope at the surface and less heat loss from the free-stream. The high regression rate keeps the thermal gradient high on the solid side, which results in more heat loss from the free-stream.

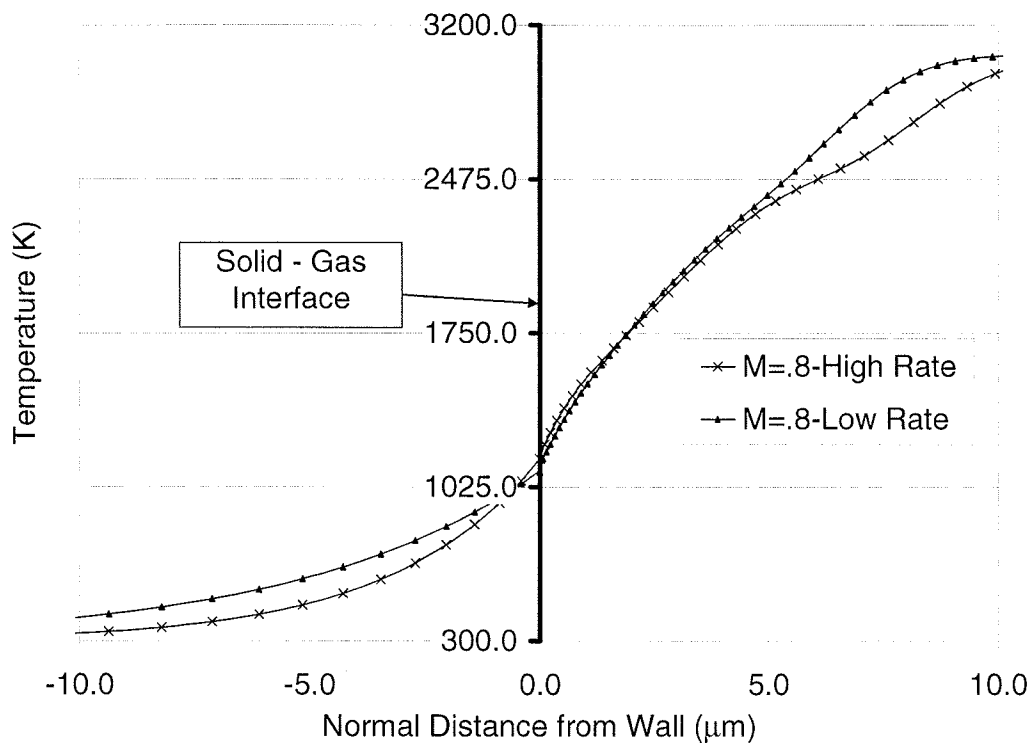


Figure 14. Comparison of Thermal Gradients at the Solid-Gas Interface for a High Rate and Low Rate Propellant

The  $r/r_o$  data generated in the analysis is verified by conducting a 1-D transient interior ballistics analysis of the high burn rate motor in question. In this analysis, the burn rate augmentation factors are simply applied by multiplying the local base rate ( $r_o = aP^n$ ) by the calculated augmentation factor as a function of the local Mach number. Figure 15 shows the results of the interior ballistics analysis compared to the static test data. The model shows a reasonable match, especially on the start-up transient when the internal  $M$ 's will be the highest.

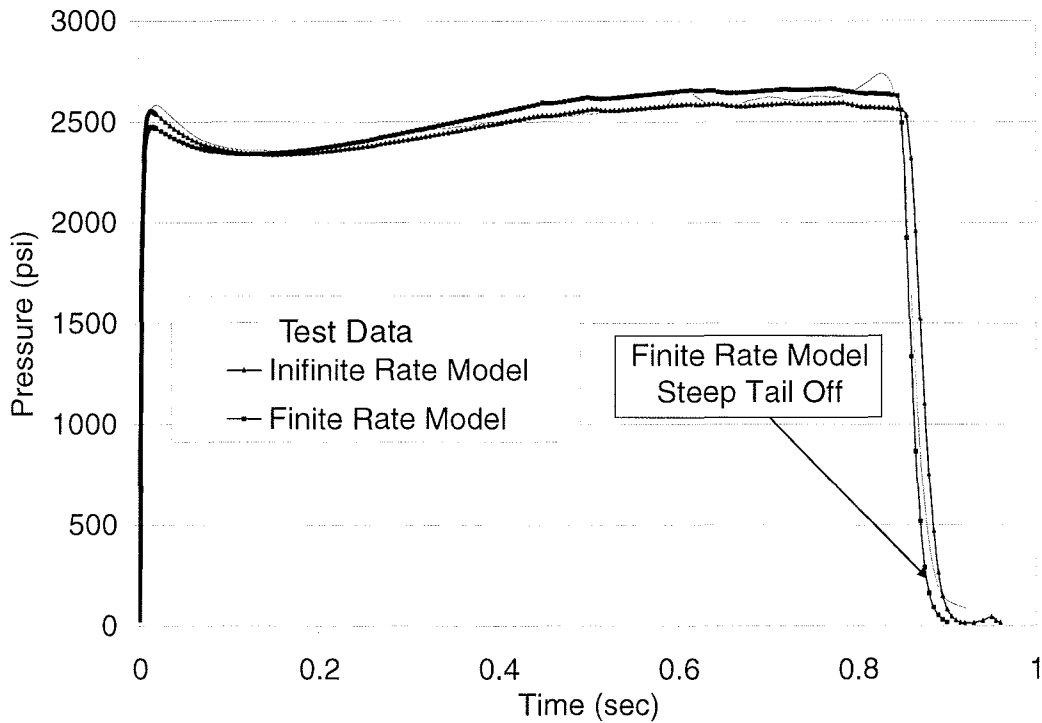


Figure 15. Interior Ballistics Results with Finite and Infinite Rate Models

The local burning rates as a function of axial distance from the head end of the motor, as calculated in the interior ballistics analysis, are shown in Figure 16 for a slice in time shortly after ignition.

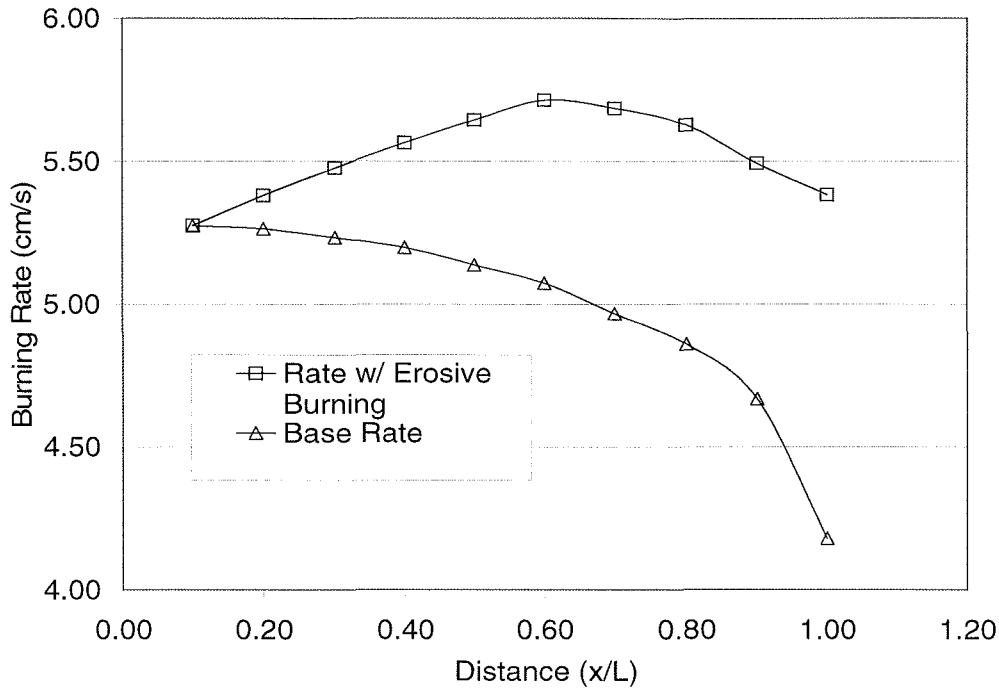


Figure 16. Erosive Burning Rate Compared to the Base Rate

The plot shows that the largest percent increase occurs at the aft end, as expected, since the aft has the highest  $M$ . However, the highest overall rate occurs at approximately  $2/3$  from the head end, where the combination of local pressure and local  $M$  combine for the largest total rate.

### C. Numerical Modeling of the 5-Inch Test Article

In similar fashion to the high rate-high shear analysis, the near-wall numerical modeling approach is used to model the geometry and propellants (burn rates) of the 5-inch test series. A series of numerical runs over a range of bulk Mach numbers (wall shear stress) are conducted for each propellant case producing and augmentation factor curve as a function of Mach number for that a particular propellant/geometry combination. EBT-3A and EBT3-B are chosen as the propellant and motor pressure conditions to model. As described in the boundary condition section, the link between the bulk Mach Number and the integral scale of the motor to the subscale model is in the application of the entrance velocity profile. A turbulent profile is assumed out to the top edge of the computational domain and will scale as the bulk Mach number for the selected integral increases (the outer physical boundary represents a  $y^+$  value that is Mach Number dependent, since the integral scale is held constant). The pyrolysis energy term is a balance between the regression rate and the heat of decomposition of the solid material. Thus, the base burning rate of a given propellant can be numerically adjusted up or down by selection of the heat of decomposition of the solid phase.

In modeling the EBT-1A and 1B configurations, two complete analyses are conducted at two values of  $h_f$  which produce two base rates near and below the EBT data. For each value of  $h_f$ , additional runs are conducted sweeping through the range of desired bulk Mach numbers. The results of these two runs are shown in Figure 17 versus the EBT-3A and 3B data. The base rates shown in the legend are referenced to EBT-3A.

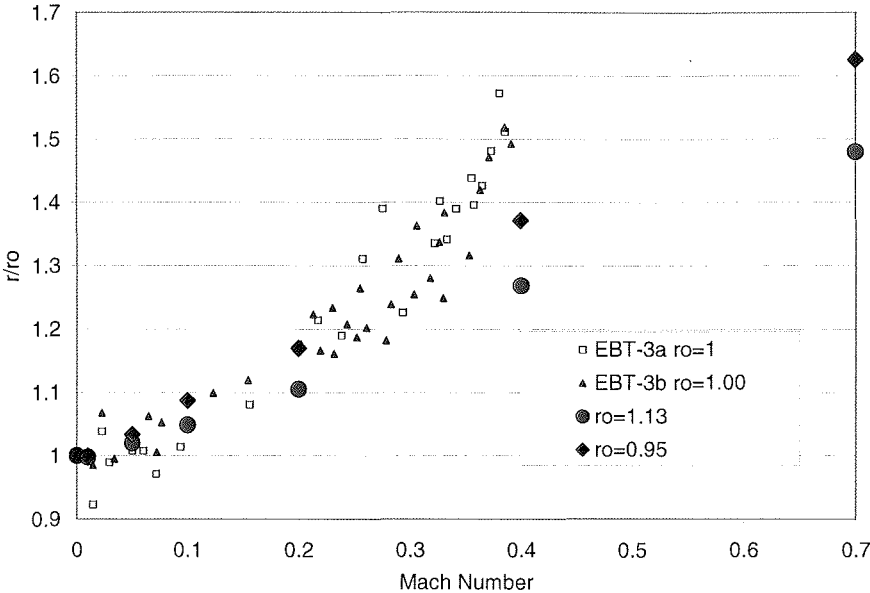


Figure 17. Comparison of Numerical Augmentation Factors to Ultrasound Test Data

The numerical data shows good agreement with test data up to approximately  $M=0.3$ . The numerical results also show the expected trend of a lowering augmentation factor as the base rate increases. The deviation at higher Mach Numbers is attributed to the variation in chamber pressure of the test data. The high Mach Number data represents the initial part of the test, while the low Mach Number data is 2.0 to 4.0 seconds later as the motor pressure changes approximately 75.0 to 100.0 psi during this interval. The numerical results are taken at constant pressure. Normalizing the test data by an average value of  $r_o$  means the slope of the normalized test data is in slight error.

#### D. Wall Momentum Ratio Definition

Also seen in the numerical results is the data point at  $M=0.01$ , which shows an augmentation factor of approximately 1.0. This indicates that the physical mechanism that contributes to the erosive burning threshold phenomenon is captured in the numerical model. Historical data shows that this threshold condition is a function of the base rate as well as the flow field conditions. As the base rate increases, the threshold condition moves to higher Mach numbers for a fixed geometry. Given that this threshold condition can be altered by either a change in the axial flow conditions or the mass injection rate, the controlling mechanism is postulated to be associated with the ratio of the axial-to-injection momentum ratio near the wall and is written as

$$\lambda = \frac{\rho U_{ref}^2}{\rho v^2} \quad (9)$$

The injection momentum can be related to the propellant burn rate by way of the continuity equation as  $\rho v = \rho_p r$ . Referencing the axial momentum in the numerator of Equation (9) to the local shear stress, the shear velocity ( $U_\tau$ ) is selected as the reference velocity. The shear velocity can be written in terms of  $\tau_w$  as

$$U_{ref} \equiv U_\tau = \sqrt{\frac{\tau_w}{\rho}} \quad (10)$$

Combining the  $U_\tau$  expression and the injection momentum in terms of the burn rate, an expression for  $\lambda$  can be written below, and is termed the wall momentum ratio

$$\lambda = \frac{\rho \tau_w}{(\rho_p r_o)^2} \quad (11)$$

Equation (11) uses  $r_o$ , the base burn rate (assumed at  $M=0.0$ ), as the reference injection momentum ratio.

The numerical data shown in Figure 17 is plotted in Figure 18 versus the  $\lambda$  function. The graph shows that the numerical data collapses to a single line when plotted as a function of the wall momentum ratio. The significance of this approach is that if the momentum ration represents a universal scaling of the data, then a universal value of  $\lambda$  exists, below which erosive burning would not be expected to occur. Note that in Figure 18, the augmentation factor begins to depart from  $r/r_o=1.0$  at a  $\lambda$  value that is approximately equal to 1.0.

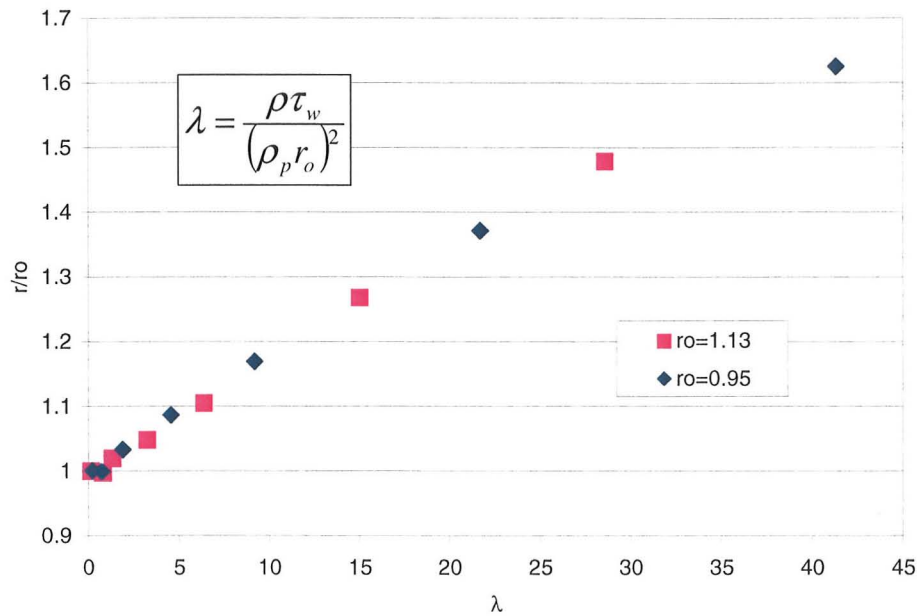


Figure 18. Numerical Augmentation Factor Versus Wall Momentum Ratio

## E. Examination of Threshold Condition

Examination of the velocity contours along the surface of the propellant for flow conditions above and below the threshold condition give insight into the contributing mechanism of the threshold condition. Shown in Figures 19 and 20 are resultant velocity vector plots for  $M=0.01$ , and  $M=0.1$ , respectively. The plots show that the flow is progressively displaced from the wall moving in the axial direction at  $M=0.01$ , while at the higher Mach Number, the plots show attachment.

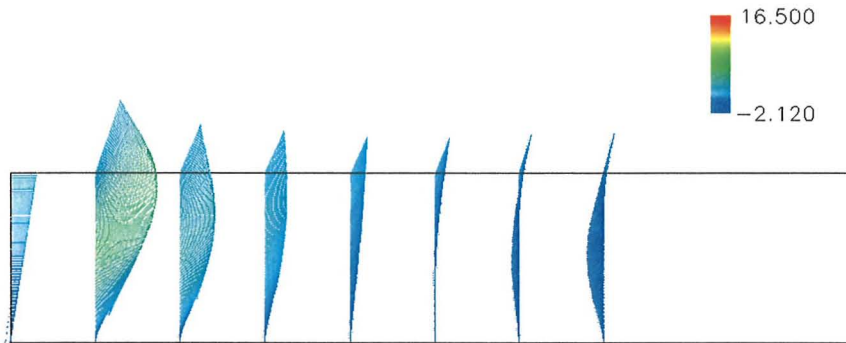


Figure 19.  $M=0.01$  Resultant Velocity Vectors

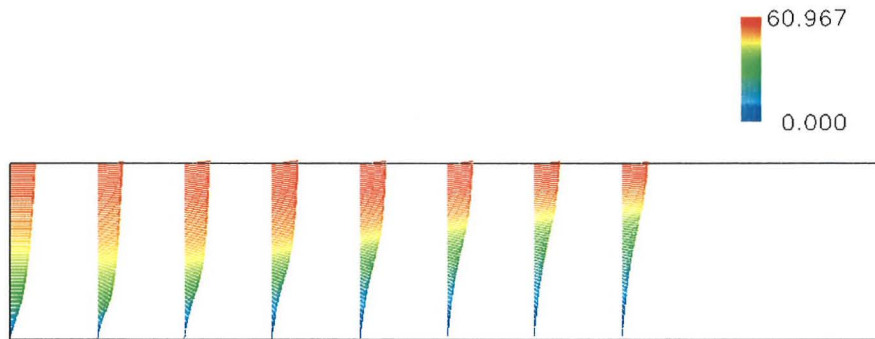


Figure 20.  $M=0.1$  Resultant Velocity Vectors

At low momentum ratios, the flow is displaced from the wall, and thus the heating conditions at the wall are dominated by normal stream lines of the injected fluid. The near-wall gradients, such as the temperature gradient, match that of the no-cross-flow case, and the resulting pyrolysis rate either matches, or in some observed cases, drops below the base rate. This correlation matches observed scaling trends that show the threshold value of Mach Number increasing with an increasing integral scale (motor diameter), or an increase in base rate. As the integral scale increases, the wall shear stress will decrease at a given bulk Mach Number condition, while a larger base rate increases the injection momentum and has the capability of displacing stronger axial flows.

## F. Wall Momentum Applied to Test Data

The correlation shown in Figure 18 is taken from a highly resolved near-wall model, using a two-step finite rate chemistry model. The wall shear stress is calculated point-by-point along the computational surface in the blowing environment. To validate the proposed wall momentum correlation, the function is applied to test data that are taken from tests of various base rates, motor pressures, and propellant types. However, no measured value of the blowing wall shear stress is available for these tests, and thus no direct means is available to calculate  $\lambda$ . If the integral scales are equal (as in the EBT testing)  $\lambda$  is assumed to scale linearly with Mach number, and inversely with the square of the base burn rates. Additional scaling is required if the solid propellant densities are not equal to the reference numerical cases ( $[\rho_p^*/\rho_p]^2$ ). Figure 21 shows that this is true for the present numerical results. In the figure, the reference data is assumed to be the numerical results  $\lambda$  (denoted with \*) for the case of  $r_o=0.95$ , with a normalized integral scale of  $Dia=1$ . Also shown are two other numerically calculated  $\lambda$ 's at  $r_o=1.13$ ,  $Dia=1.0$ , and  $r_o=1.43$ ,  $Dia=41.2$ . Two scaled curves are also plotted that are derived from the assumed reference curve using the scaling law in Equation (12). Figure 7 shows excellent results when scaling data from like integral scale, but not between different integral scales. This is expected because the scaling law that is used operates only on the denominator on the  $\lambda$  function, yet the shear stress in the numerator is not constant across integral scales at like Mach Numbers.

$$\lambda(M) = \lambda^*(M) \left( \frac{r_o^* \rho_p^*}{r_o \rho_p} \right)^2 \quad (12)$$

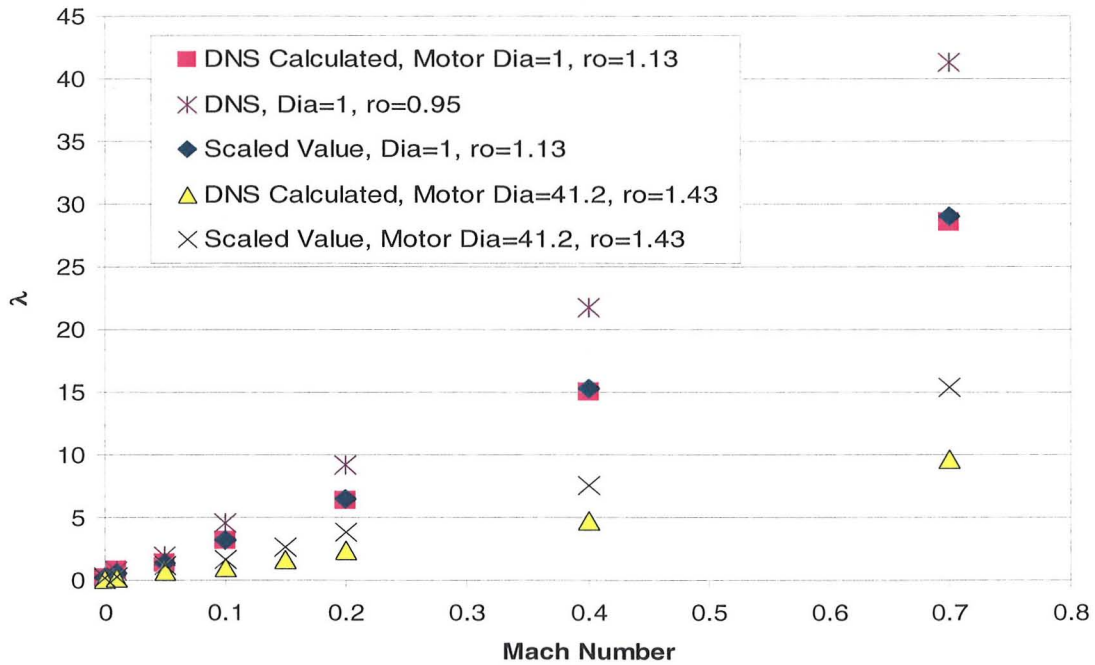


Figure 21. Calculated  $\lambda$  Function Versus Mach Number

Given that all of the EBT data is at the same integral scale as the numerical data, Equation (12) is used to derive a  $\lambda$  function for each of the tests by scaling the reference numerical data. The test data is plotted in Figure 22 as a function of the derived  $\lambda$ . Note that the data in these tests represent three different propellants with normalized base burn rates and average chamber pressures ranging from 0.73 to 1.13. Two different binders are represented as well. Best linear fits are shown over the data to accentuate the grouping of the data. Figure 23 repeats the data shown in Figure 1 with best linear fits shown as well. A comparison between the two plots shows considerable improvement on the grouping of the data.

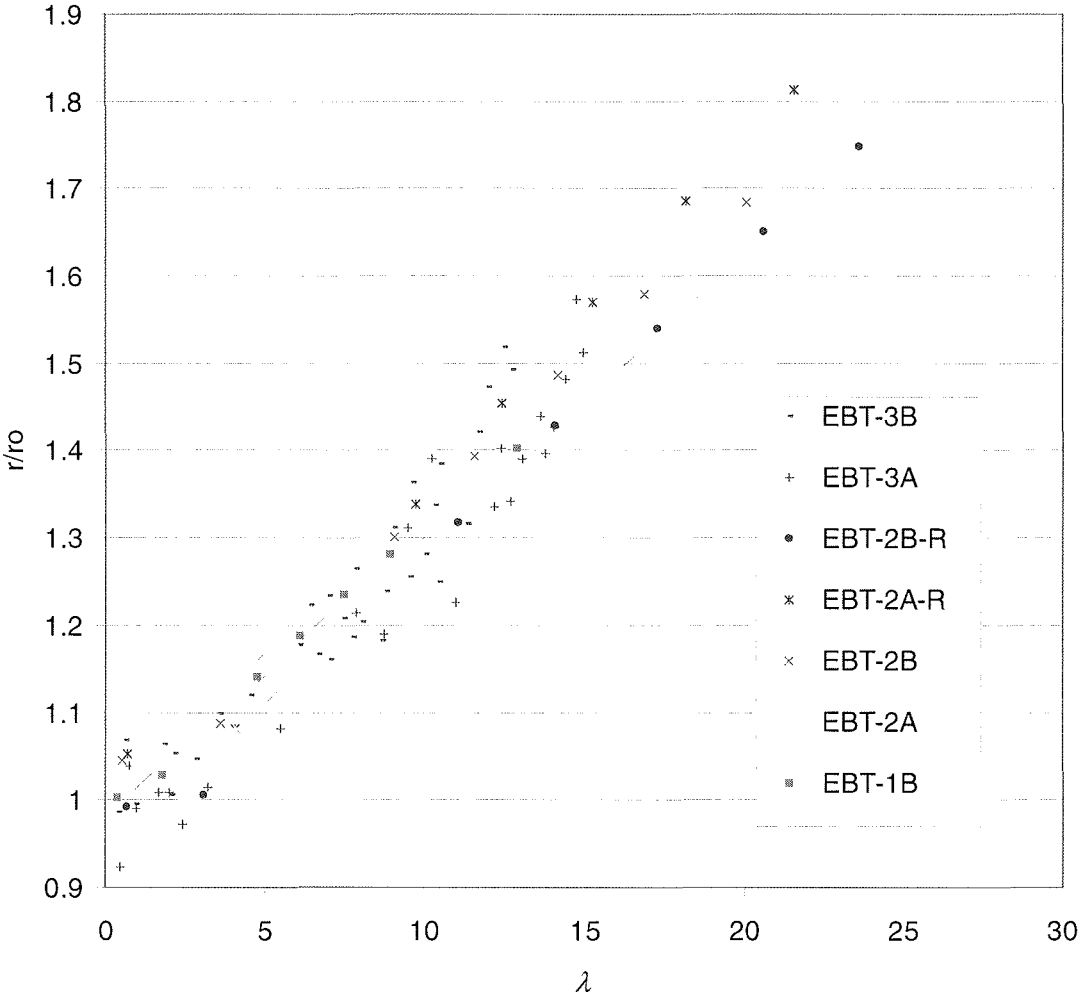


Figure 22. EBT Test Data Augmentation Factor's Versus Derived  $\lambda$  Function

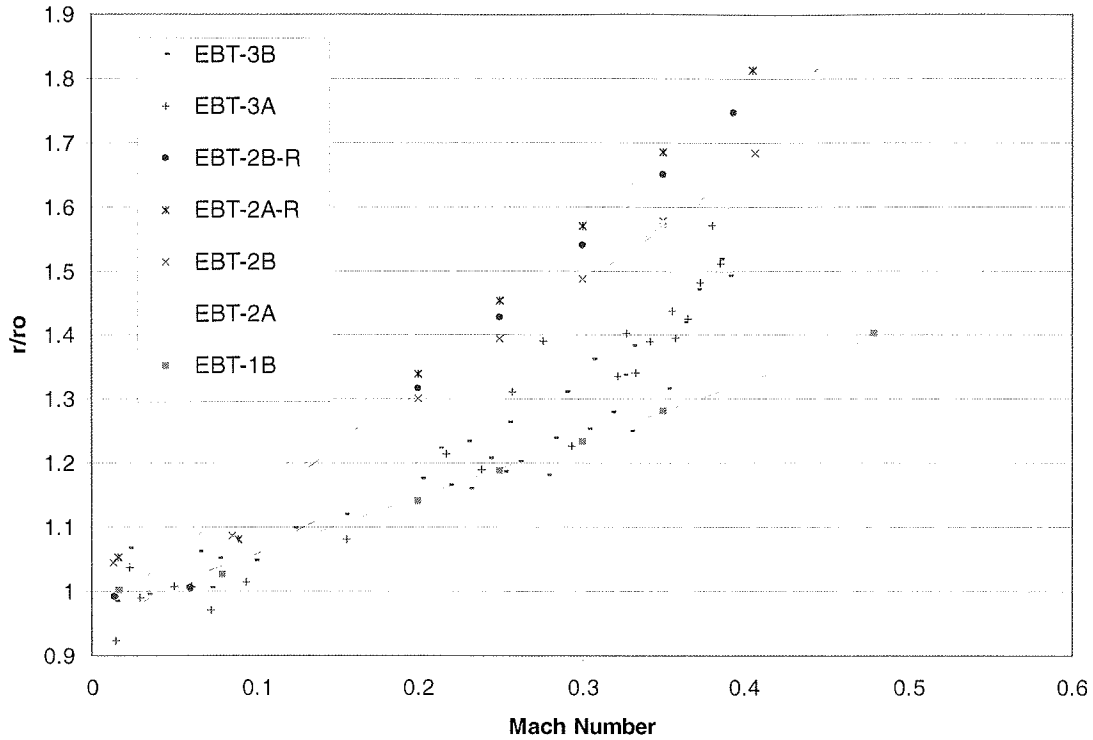


Figure 23. EBT Test Data Augmentation Factor's Versus Mach Number

### G. Integral Scaling of Wall Momentum

Because all of the EBT testing was conducted at a constant integral scale, no determination can be made as to the constancy of  $r/r_o$  versus  $\lambda$  for different motor diameters. The scaling with integral scale is presumed to be through the wall shear stress. Historically, erosive burning data that is viewed in the Mach number realm shows a decrease in the augmentation factor and a shift upward in the threshold value as either the motor diameter increases or the base rate increases. Both effects are contained in the  $\lambda$  function. To examine the impact of the integral scale on the correlation of  $r/r_o$ , the present numerical technique is applied to two hypothetical motors with integral scales that are  $\sim 41$  times greater than the test data. As seen in Figure 24, when  $r/r_o$  is viewed in terms of Mach number, the data trends are as expected. The threshold value moves higher, and the augmentation factors at a given Mach number drop for the high rate, large scale case. The combination of the higher injection rate (higher base rate) and the reduced shear stress at the larger integral scale, reduce the augmentation as a function of Mach number. Note in Figure 24 that the threshold value has pushed beyond  $M=0.1$ . The augmentation factors drop for the large scale case with the lower rate as compared to the case of comparable rate and smaller scale, again reflecting the reduced shear stress effect. The augmentation factors are now plotted as a function of  $\lambda$  in Figure 25 for all four simulations. The larger integral scale data tends to the same line as does the lower integral scale data, and the threshold points remain in the vicinity of  $\lambda \sim 1.0$ .

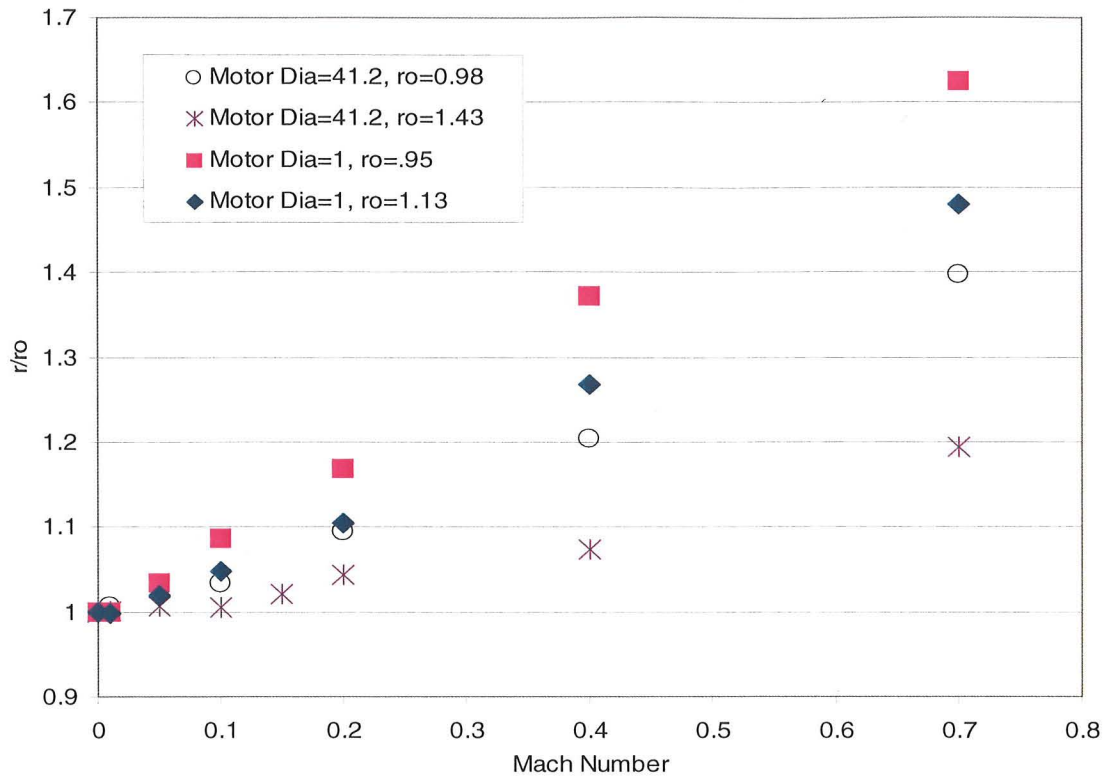


Figure 24. Effect of Integral Scale on Augmentation Factors

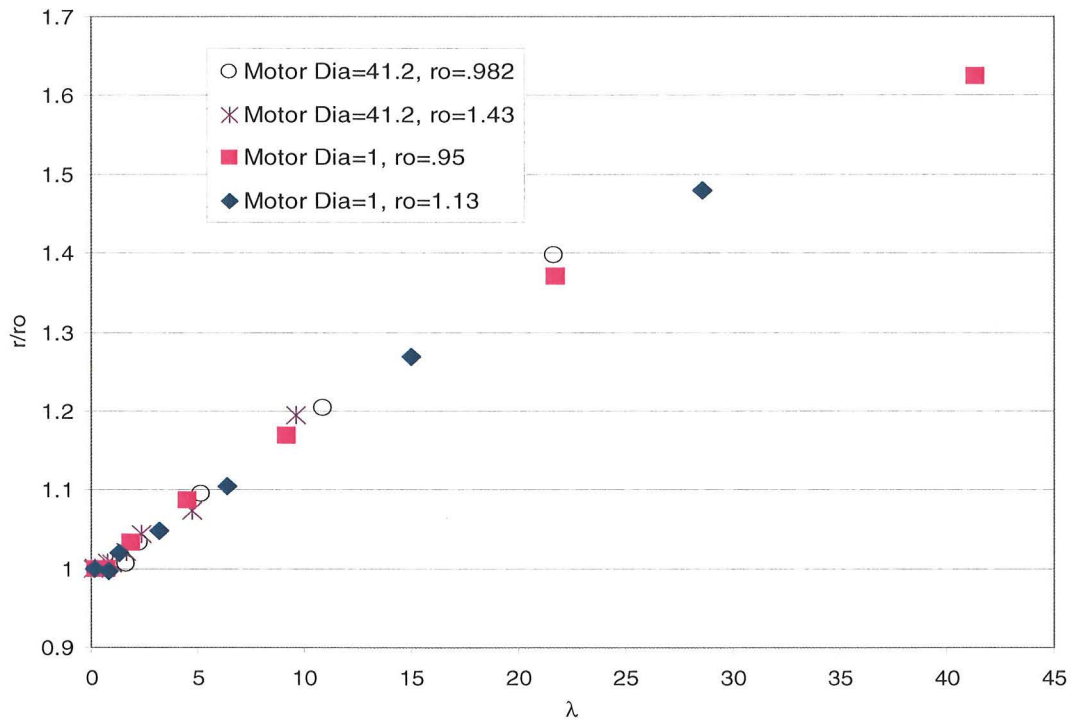


Figure 25. Effect of Integral on Correlation of Augmentation Factors to  $\lambda$

## H. Observation of The Wall Momentum Function

The pyrolysis rate of a solid propellant can be viewed on the most fundamental scale as a heat transfer problem. The combustion process is indeed part of the heat transfer problem in establishing heat release locations and small scale turbulence in the near-wall region. However, the present numerical results and a comparison to test data indicate that the primary controlling variables for erosive burning are gas dynamic parameters. Based on the analysis results, the film layer compression due to cross-flow and the film layer displacement due to mass injection are proposed as primary physical mechanisms controlling erosive burning. The momentum of these two streams competes to establish the heat transfer from the combustion zone and the free stream back to the regressing propellant surface. The surface momentum ratio ( $\lambda$ ), as defined in this report implicitly contains all of these parameters. Plotting both numerical and test data versus this parameter shows good agreement.

The highly resolved, reacting flow model used in this analysis has shown that the augmentation factor ( $r/r_0$ ) can be successfully correlated to the wall momentum ratio, across propellant types, base rates, and integral scales. The numerical results, in terms of Mach number, are shown to be in good agreement with ultrasound data taken on burning propellant grains. The significance of this correlation is twofold. Firstly, using  $\lambda$  as a universal scaling parameter allows for the translation of test data from one base rate to another for a fixed integral scale. Secondly, test data can be translated from one integral scale to another as a function of Mach number, provided that the true wall shear stress (to include blowing effects) is available. The effect of motor pressure is inherently contained in the  $\lambda$  correlation through the wall shear stress, and the base burning rate ( $aP^n$ ) which means pressure scaling is contained in the function.

The numerical results show the ability to capture the threshold condition for erosive burning as a function of Mach number. A review of test data shows that this condition scales with the parameters that are contained in  $\lambda$ . For a fixed geometry, the threshold conditions will move out to higher Mach numbers as the base rate is increased, and for a fixed base rate, the threshold will move out as the hydraulic diameter increases. Both of these phenomenons are seen in the numerical results as presented in Figure 24. However, when plotted versus the  $\lambda$  function, the threshold conditions appear to remain in the vicinity of  $\lambda = 1.0$ , which is proposed here as an approximate universal threshold condition. The numerical results suggest that the threshold condition corresponds to the point where sufficient axial momentum is available to keep the film layer attached to the propellant surface.

Referencing the axial momentum to the shear velocity, and thus the shear stress, has the advantage of linking results of the highly resolved model to full motor CFD. Presently, the augmentation factor- $\lambda$  function is being incorporated as a boundary condition in rocket motor CFD analysis. The local blowing shear stress is calculated allowing for the calculation of a local  $\lambda$ . The augmentation factor is then multiplied by the local  $r_0=cP^n$  to find the mass injection boundary condition of the burning propellant.

## V. WALL MOMENTUM RATIO MACRO MODEL FOR INTERIOR BALLISTICS

Based on the hypothesis that the erosive burning mechanism and the threshold mechanism are physically related, and that both are strongly influenced by the competing momentum streams at the surface of the propellant, the wall moment function is examined as a universal correlation variable for the erosive burning augmentation factor and the threshold condition.

As Equation (11) shows, the numerator of the wall momentum function contains the product of the gas density and the local wall shear stress. The correlation shown in Figure 18 is derived from a highly resolved near-wall model with the velocity gradient evaluated from grid points within  $10.0 \mu m$  from the wall which is below the primary flame of composite solid propellants (decomposed AP, and binder) and well within the influence of the injection gas or blowing wall. This implies that to make use of the strong correlation shown in Figure 18, a highly resolved model must be constructed, which then negates the advantage of the universal correlation of  $r/r_o$  because  $r/r_o$  would then be available from the numerical calculations.

To take full advantage of the  $\lambda$  correlation,  $\lambda$  must be available through global scaling parameters, such as the free stream velocity ( $U_m$ ), a reference diameter ( $D_{ref}$ ),  $r_o$ , the Reynolds Number ( $Re$ ), and  $\tau_{w-NB}$ , where  $\tau_{w-NB}$  is the wall shear stress for a non-blowing wall. Correlations for the non-blowing wall shear stress in terms of the local Reynolds number are widely documented. Ultimately, the objective is to demonstrate a universal correlation that will relate a non-blowing wall momentum function to a blowing wall momentum function, such that the correlation in Figure 18 may be used in the design phase of solid propellant rocket motor grains. The results presented in this section demonstrate a suitable universal correlation of the blowing to non-blowing  $\lambda$  which is then used to develop a universal erosive burning scaling law. The scaling law predictions are compared to ultrasound test data, as well as used to calculate motor head end pressure for comparison to test data.

### A. Development of the Wall Momentum Macro Correlation

The development of the correlation begins by curve fitting the data presented in Figure 18. When this data is plotted as  $(r/r_o)^{2.69}$ , the result is a straight line as shown in Figure 26. Plotting the data in the form a straight line allows for confident extrapolation beyond the current numerical data base.

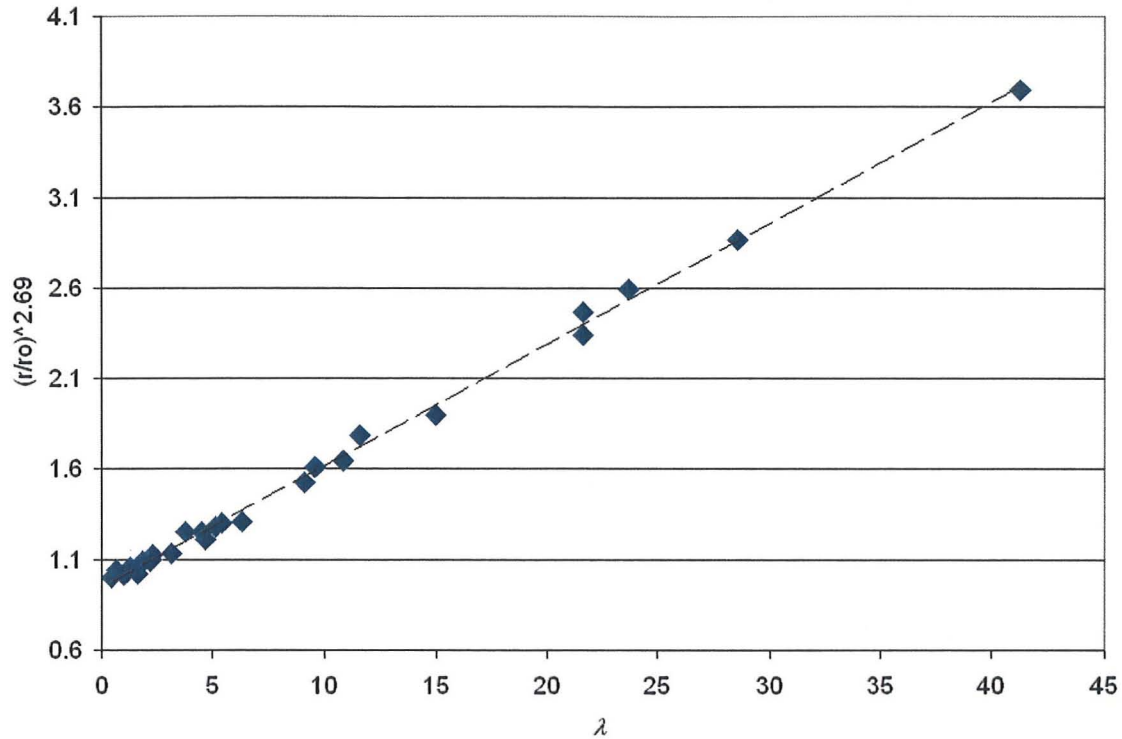


Figure 26. Linear Curve Fit of  $(r/r_o)^{2.69}$  versus  $\lambda$

Equation (13) represents a linear curve fit of the data and has an  $R^2=0.997$  ( $R^2$  is Pearson's Coefficient of Regression).

$$\left(\frac{r}{r_o}\right)^{2.69} = 0.06693\lambda + 0.9464 \quad (13)$$

The non-blowing  $\lambda$  is defined in terms of the free stream density and the local non-blowing shear stress as shown in Equation (14). The relationship between the shear stress and the local skin friction coefficient is shown in Equation (15). The local skin friction coefficient,  $\gamma$ , is calculated from Prandtl's universal law of friction for a smooth pipe, which is shown in Equation (16).

$$\lambda_{NB} = \frac{\rho_m \tau_{wNB}}{(\rho_p r_o)^2} \quad (14)$$

$$\gamma = \frac{\tau_{wNB}}{\left(\frac{1}{2} \rho_m U_m^2\right)} \quad (15)$$

$$\frac{1}{\sqrt{\gamma}} = 4.0 \log_{10}(\text{Re} \sqrt{\gamma}) - 0.4 \quad (16)$$

Five test motor configurations are selected for analysis in the development of the universal scaling law based on  $\lambda_{NB}$ , and  $\lambda$ . These motors have a wide range of base burning rates, integral scales, and flame temperatures. Each of the test cases has considerable data that can be used either directly or indirectly for validation of the resulting scaling law. Table 3 shows the normalized characteristics of the test motors. Notice that motor 5 represents an extreme deviation in base burn rate from the other four motors, while test motors 3 and 4 represent an extreme deviation in integral scale. All data are normalized by motor 1.

Table 3. Normalized Characteristics of the Test Motors

Motor	Base Burn Rate $r_o/r_{o-ref}$	Integral Scale $D/D_{ref}$	Flame Temperature $T_F/T_{F-ref}$	Head End Chamber Pressure $P/P_{ref}$
1	1.00	1.00	1.00	1.00
2	1.19	1.00	1.00	1.00
3	1.51	41.21	1.00	1.00
4	0.99	41.21	1.00	1.00
5	6.05	0.33	0.89	3.51

Using Equations (14-16), the non-blowing wall momentum function is calculated for test motors 1 through 4, along with the non-blowing shear velocity ( $U_{SH} = \sqrt{\tau_{NB}/\rho_m}$ ). A set of numerical calculations is performed for each of these four motors to find the blowing  $\lambda$  values over a range of bulk Mach numbers. The numerical results are shown in Figure 27 as the ratio of  $\lambda/\lambda_{NB}$  plotted as a function of the shear Mach Number ( $M_{SH}$ ), which is defined as the ratio of the shear velocity to the bulk speed of sound. The curve shows two distinct groupings that are dominated by the integral scale of the motor.

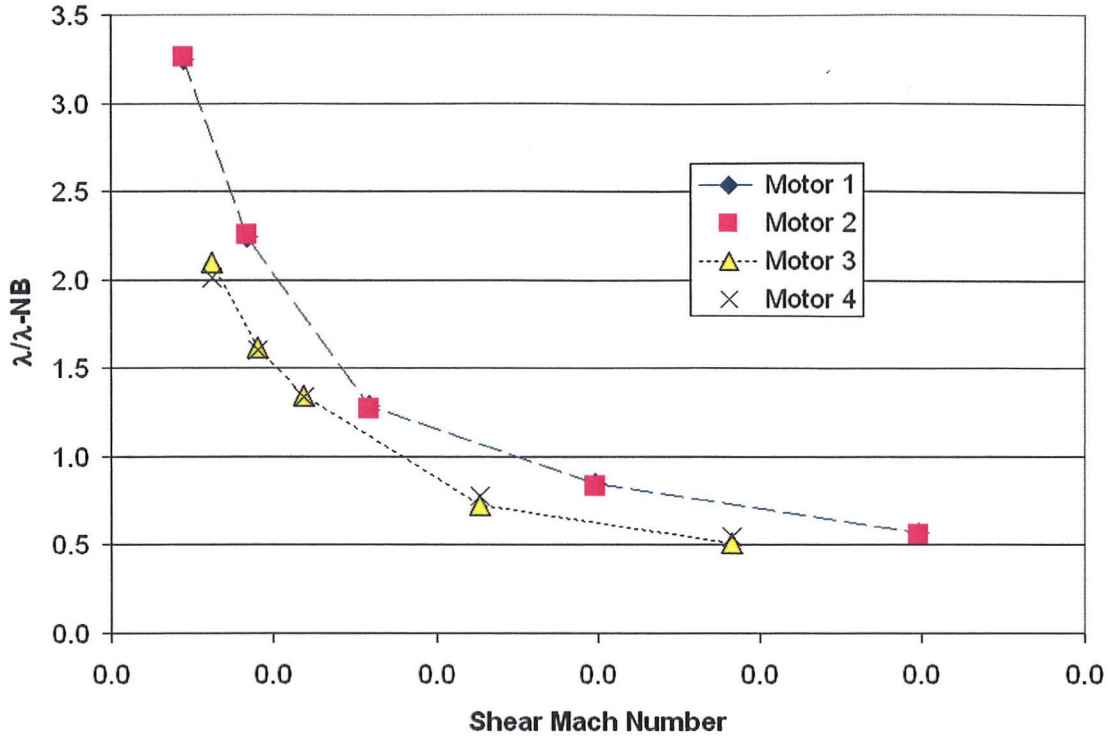


Figure 27. Ratio of Blowing to Non-Blowing  $\lambda$  Versus Shear Mach Number

The true wall shear stress is assumed to vary with the integral scale and the gas injection velocity at the wall, with both quantities influencing the wall shear stress in the same manner. The wall shear stress decreases as the integral scale or the injection velocity increase. Therefore, the blowing  $\lambda$  is assumed to be related to the non-blowing  $\lambda$  by some function of  $r_o$ , and  $D_{ref}$ . Desiring a nondimensional function of these two variables, the Reynolds number based on the injection velocity ( $Re_i$ ) is defined in Equation (17). The proposed correlation function is shown in Equation (18), and is plotted versus the shear Mach number in Figure 28. By trial and error, the strongest correlation of the data occurs when  $\kappa=0.067$  which is used in Figure 5.

$$Re_i = \frac{\rho_p r_o D_{ref}}{\mu} \quad (17)$$

$$\Lambda_{EB} = \left( \frac{\lambda}{\lambda_{NB}} \right) (Re_i)^\kappa \quad (18)$$

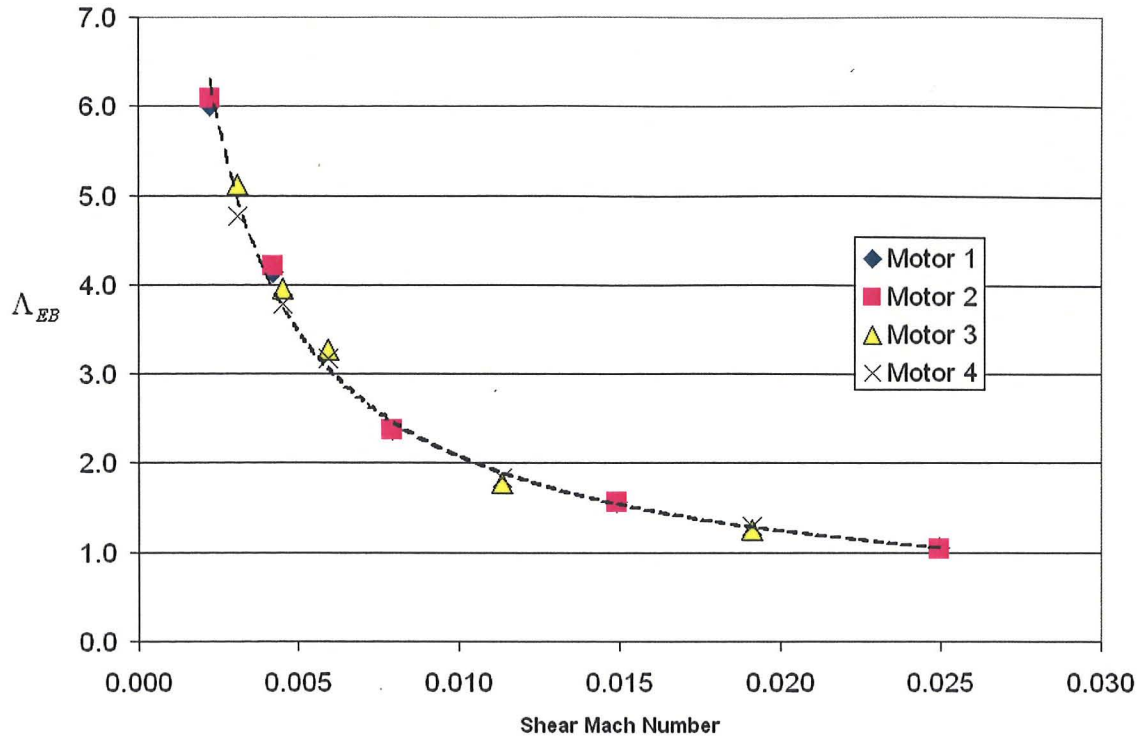


Figure 28. Correlation of  $\lambda$  Function to Shear Mach Number

In Figure 28, the data is curve fit using a power law function ( $R^2=0.995$ ). The resulting curve fit is shown in Equation (19).

$$\Lambda_{EB} = 0.0652M_{Sh}^{-0.7517} \quad (19)$$

By combining Equations (13) and (19), the augmentation factors versus bulk Mach number can be calculated from global design variables of a rocket motor. The bulk Mach number is converted to a bulk velocity and Reynolds Number for the integral scale of the motor. The non-blowing shear stress is calculated using the Prandtl equation in Equation (16), from which the non-blowing shear velocity and shear Mach number can be found. Equation (19) is used to find the  $\Lambda_{EB}$  and then converted to  $\lambda$  by way of Equation (18). Finally, Equation (13) is used to find the augmentation factors,  $r/r_o$  from the calculated  $\lambda$ .

## B. Macro Model Validation

Validation of the proposed universal scaling law for erosive burning is demonstrated in two ways. Firstly, the scaling law is used to predict the augmentation factors for several motors that have ultrasound measured burn rate information available. This set of motors has equal integral scales, but different base burn rates and propellant formulations. In addition, two different binder systems are represented in the formulations. The second approach is to predict the augmentation factors versus Mach number for Motor 5 in Table 3 using the scaling law, and use this function in an interior ballistics prediction of the motor's head end pressure. This prediction is compared to test data. All geometry and base burn rate scaling shown in the figures are referenced to Motor 1 in Table 3.

Figures 28 through 30 show comparisons of the universal scaling as compared to ultrasound data for three motor configurations. The ultrasound data are taken over a period of time of the motor operation during which the chamber pressure is not constant, thus neither is the base rate. As such, the normalization of  $r$  in this data is by an  $r_o$  value that occurs when the Mach Number decays to approximately zero, and is thus the base rate at the local instantaneous pressure. Since the higher Mach number data is taken at an earlier point in time and a different chamber pressure, the normalization of these numbers is slightly in error. The magnitude of this error is considered small, but it does cause a trend in the data that deviates slightly from linear. This is most pronounced in Figure 30, where the mid-Mach number data deviates considerably from a linear progression. The data in Figures 28 and 30 are for PBAN binder systems, while the data in Figure 29 is for an HTPB system. Figure 29 represents the lowest base rate test case which corresponds to the highest  $\lambda$  values. The  $\lambda$  value at  $M=0.7$  is equal to 65.9 which falls beyond the numerical data in Figure 18, and as such represents an extrapolation of the numerical data. However, the data point falls in line with the values calculated within the numerical data base. The scaling law data in the figures below are referenced to a pressure and corresponding base rate ( $aP^n$ ) that matches the  $r_o$  used to normalize the ultrasound data for each case. The comparisons show very good agreement across both binder systems.

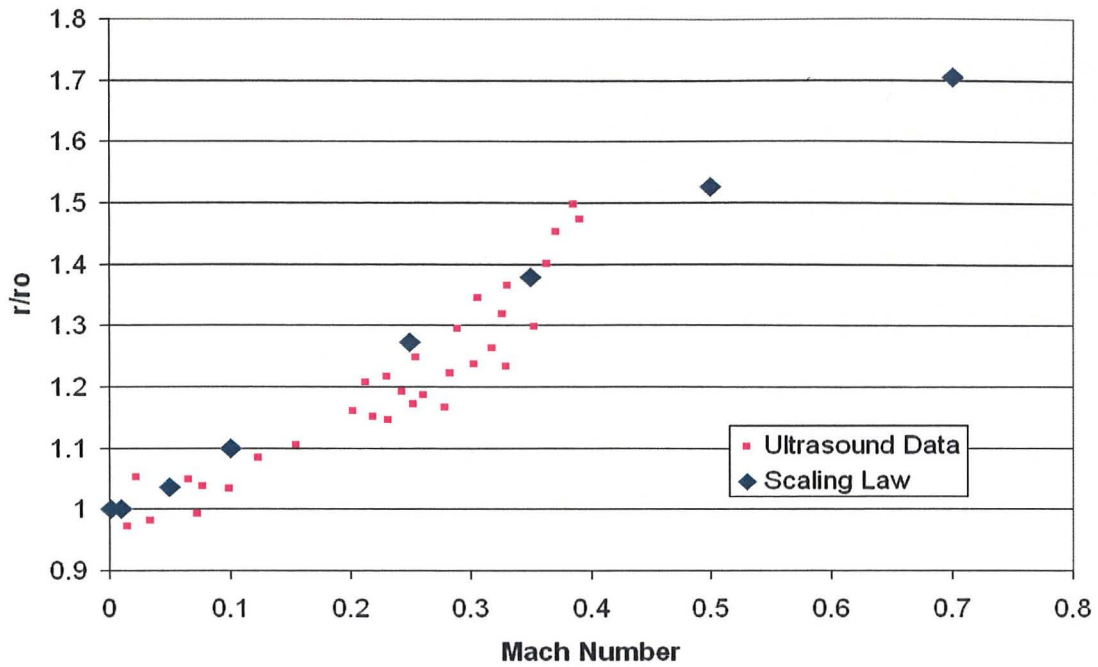


Figure 29. Augmentation Factor Versus Mach Number  
 ( $r_0/r_{0-ref}=1.072$ ,  $D_0/D_{0-ref}=1.0$ , PBAN Binder)

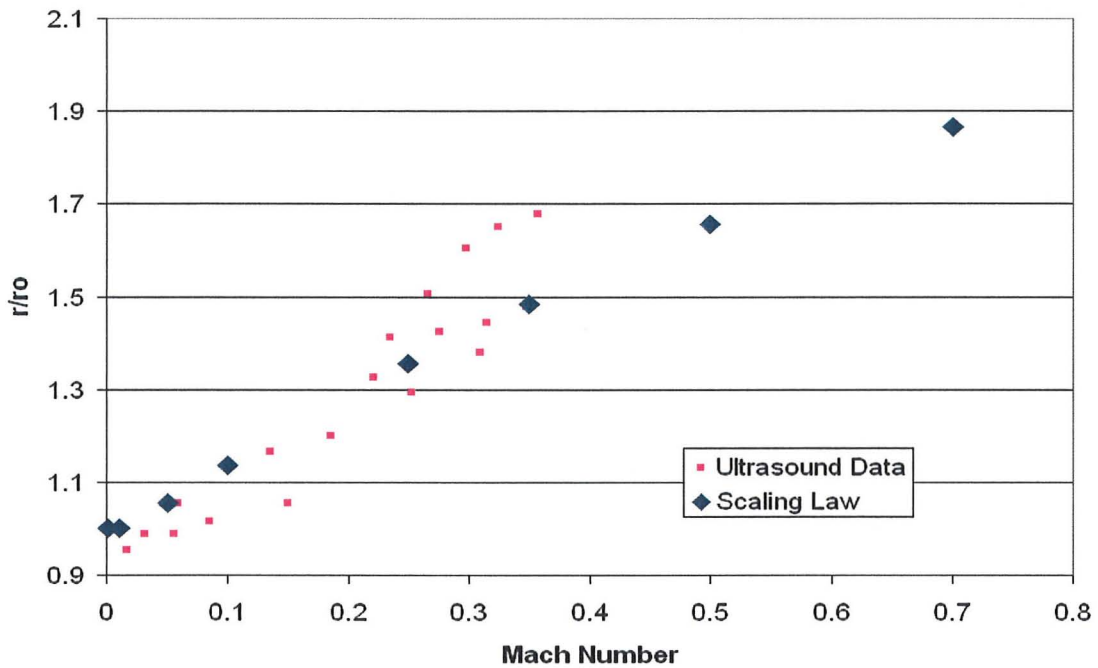


Figure 30. Augmentation Factor Versus Mach Number  
 ( $r_0/r_{0-ref}=0.830$ ,  $D_0/D_{0-ref}=1.0$ , HTPB Binder)

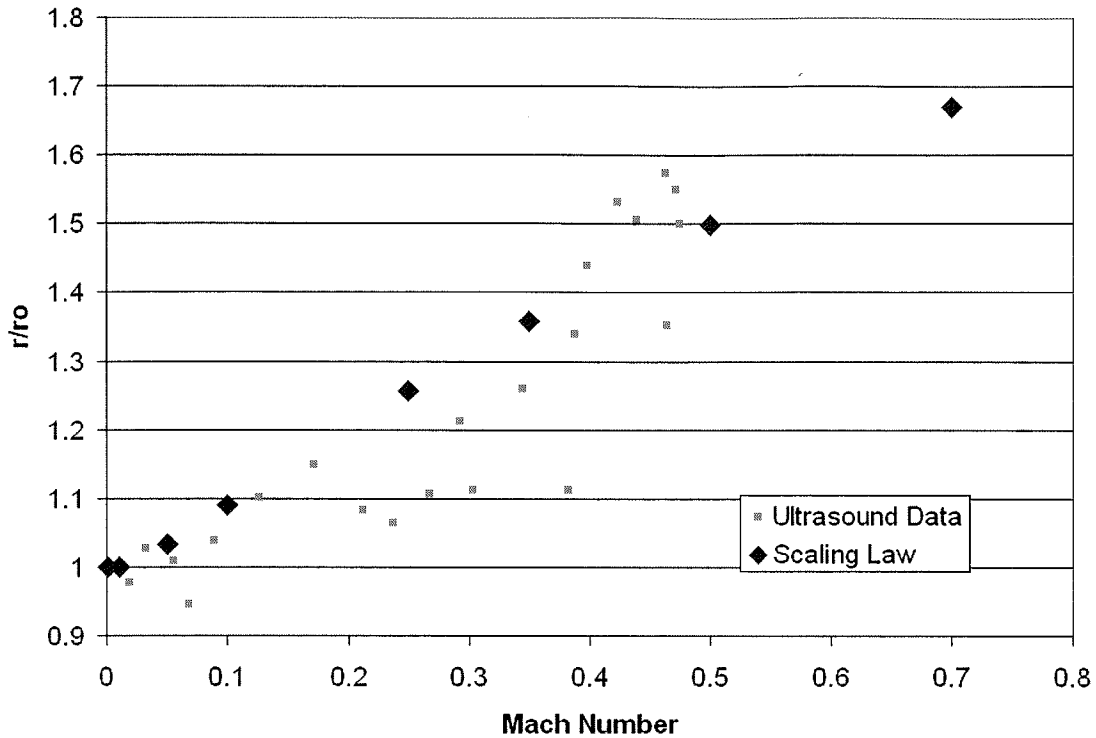


Figure 31. Augmentation Factor Versus Mach Number  
 ( $r_o/r_o\text{-ref}=1.20$ ,  $D_o/D_o\text{-ref}=1.0$ , PBAN Binder)

Shown in Figure 32 are scaling law data compared to numerical data for motor 5 in Table 3. Motor 5 represents a unique test of the scaling law because both the integral scale and the base rate deviate considerably from the previous validation cases. The numerical data and the interior ballistics analysis results shown in Figure 33 were previously shown as demonstrations of the numerical approach to erosive burning (**Wall Momentum – C. Numerical Modeling of a High Burn Rate-High Shear Geometry**). Figure 33 shows test data for the head end pressure of this high burn rate motor. Also shown are the interior ballistics results with and without the erosive burning model. The results in Figure 33 were generated with the numerical data implemented as a function of Mach number as shown in Figure 32. The scaling law data shown in Figure 32 is in excellent agreement with the numerical model, and is thus expected to produce identical results in an interior ballistics analysis.

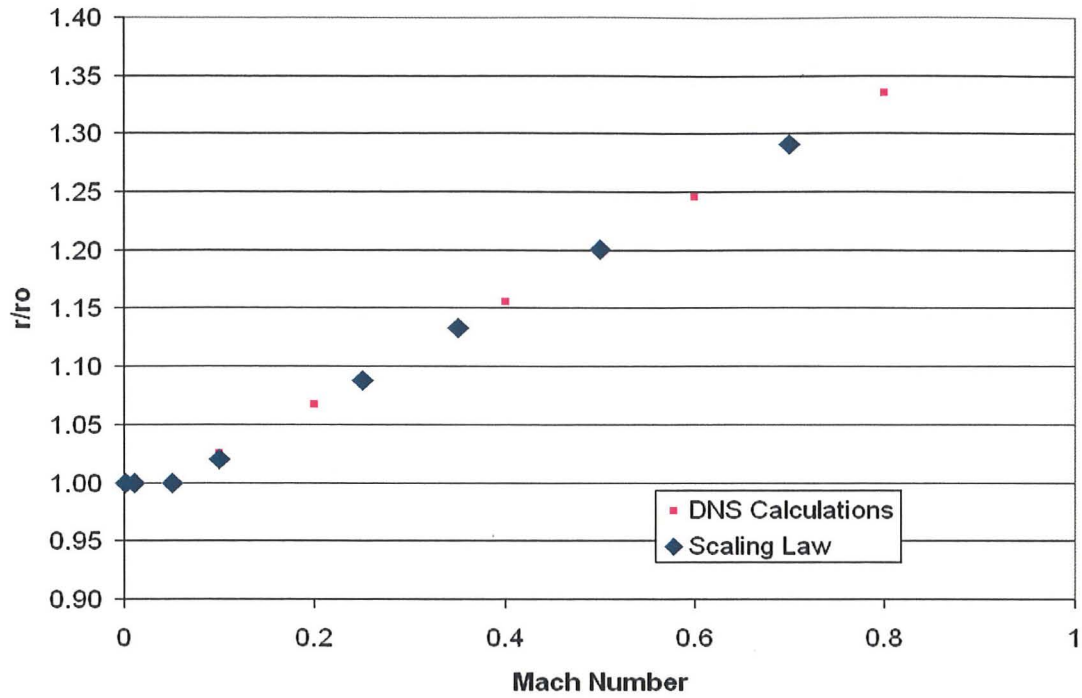


Figure 32. Augmentation Factor Versus Mach Number  
 ( $r_o/r_{o-ref}=6.05$ ,  $D_o/D_{o-ref}=0.333$ , HTPB Binder)

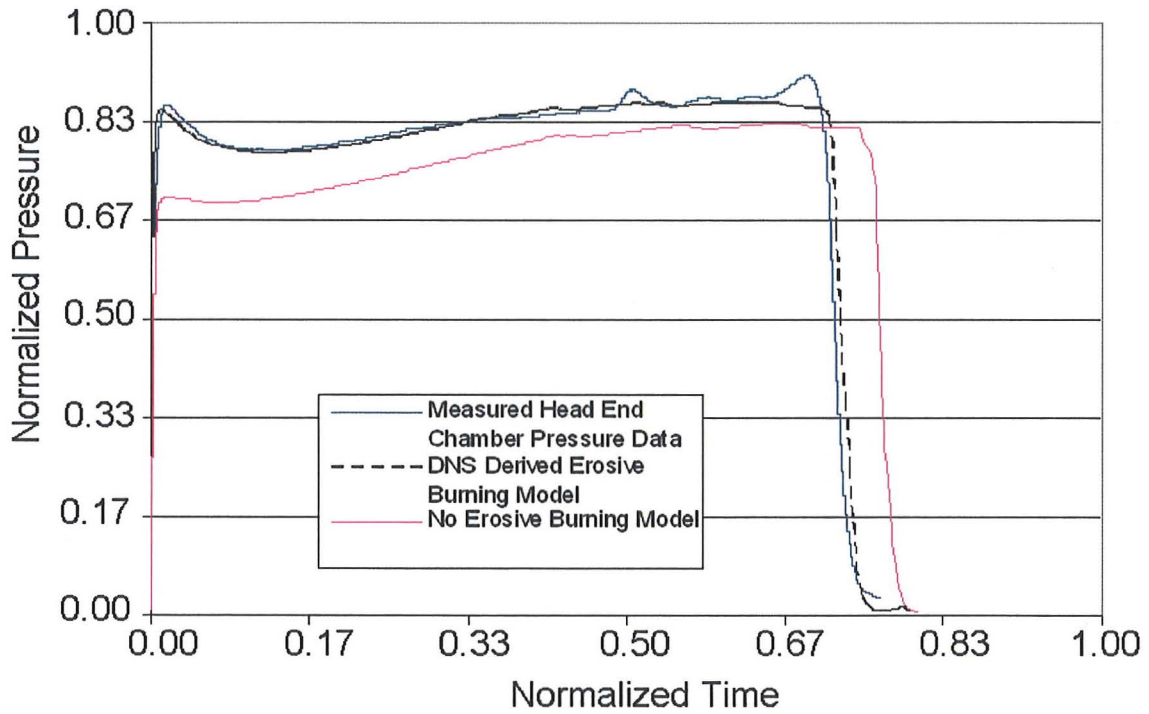


Figure 33. Interior Ballistics Analysis Results for Motor 6

### C. Observations and Conclusions on the Wall Momentum Macro Model

The correlation of the augmentation factors to the wall momentum ratio shows a universal correlation, but is inconveniently associated to the blowing wall shear stress. The results in this report have demonstrated that a universal correlation between the blowing and non-blowing wall shear stress exists. Because the non-blowing shear stress can be calculated from existing correlations, the correlation of  $\lambda$  to  $r/r_o$ , and the correlation of the blowing to non-blowing shear stress are combined to produce a universal scaling law of the erosive burning augmentation factors. This scaling law has been demonstrated over a wide range of base burning rates and integral scales, as well as different binder systems. The targeted application of this scaling law is internal ballistics design codes where the flow field is approximated as 1-D. In these applications, the global parameters used in the scaling law are readily available. The present results show that this law may be of greater accuracy than previous correlations used in the 1-D context. However, in highly 3-D regions of a propellant grain, the proposed correlation may be inadequate in predicting erosive burning. Given this caveat, the resulting scaling law can be used as a design guide in avoiding or predicting erosive burning magnitudes during the early development phase of a rocket motor design.

## VI. CONCLUSIONS

The primary objective of this work is to develop an erosive burning scaling law and model that can be useful to the design interior ballisticians as a predictive tool. Several erosive burning models have existed for years, but all fail to adequately scale across a wide range of burning rates and motor geometries. Through the use of highly resolved near-wall numerical modeling, a scaling law has been observed which suggests that the primary controlling mechanism for the onset and magnitude of erosive burning can be seen as a competition between the cross-flow momentum and the injection momentum. The purpose of the near-wall analysis is not to study the in-depth nuances of the AP-binder combustion process, but to incorporate sufficient physics into an analysis that demonstrates the dependency of the mass injection or pyrolysis rate on near-wall injection and cross-flow interactions. The study also serves to give physical insight into the “threshold” condition for the onset of erosive burning. At low cross-flow momentums, the injection momentum can lift the boundary layer and alter the thermal gradient or heat transfer into the solid.

The  $\lambda$  function is a useful boundary condition for CFD analyses that do not resolve the flame structures. CFD models that treat the wall region with sufficient resolution to obtain the blowing wall shear stress can use  $\lambda$  to account for the erosive contribution to the local propellant burning rate. However, for the scaling law to be useful to the ballisticians, the erosive burning model must be cast in terms of flow and geometry parameters that are readily available from 1-D analysis. The wall momentum macro model has been demonstrated to bridge the gap between the subscale analysis and the interior ballistics code.

There are several assumptions and simplifications that have been incorporated into the methods that produced the presented results. The near-wall analysis is based upon a two-flame, 2-D analysis. In general, the AP-binder is considered to be at least a three-flame process, and turbulence is a 3-D phenomenon. More detailed analyses exist that explore these effects further. However, the verification problems used for demonstration of the wall momentum function based on the present level of detail show that the developed correlations match test data very well, specifically in regards to predicting motor head end pressure via interior ballistics. From this one may draw the conclusion that, although several details are lacking in the near-wall analysis, the present models contain the dominant factors that control the erosive burning mechanism.

## REFERENCES

1. Isfahani, A., Zhang, J., and Jackson, T., "The Effects of Turbulence-Induced Time-Periodic Shear on a Flame Anchored to a Propellant," *Combustion and Flame*, Vol. 156, Issue 5, May 2009, pp. 1084-1098.
2. McDonald, B., "Numerical Analysis of the Correlation of Erosive Burning and the Threshold Condition in Solid Propellants Using the Wall Momentum Ratio," *JANNAF Journal of Propulsion and Energetics*, May 2008.
3. McDonald, B., "Global Scaling of the Wall Momentum Function for an Erosive Burning Prediction Correlation," *JANNAF Journal of Propulsion and Energetics*, April 2009.
4. Sutton, George P., *Rocket Propulsion Elements* (John Wiley and Sons, New York, 1967).
5. King, Merrill K., "Erosive Burning of Solid Propellants," *Journal of Propulsion and Power*, Vol. 9, No. 6, 1993, pp. 785-805.
6. Wang, Qunzhen, 2003, "Development of Erosive Burning Models for CFD Predictions of Solid Rocket Motor Internal Environment," *39<sup>th</sup> AIAA/ASME/SAE/ASEE Joint Propulsion Conference and Exhibit*, AIAA 2003-4809, July 2003.
7. Bulgakov, Victor K., and Karpov, Alexander I., "Numerical Studies of Solid Propellant Erosive Burning," *Journal of Propulsion and Power*, Vol. 9, No. 6, 1993, pp. 812-818.
8. Vilynov, V. N., "On the Theory of the Erosive Burning of Powders," *Doklady AN SSSR*, Vol. 136, No. 2, 1961, pp.381-383.
9. Gordon, J.C., Duterque, J., and Lengelle, G., "Erosive Burning in Solid Propellant Motors," *Journal of Propulsion and Power*, Vol. 9, No. 6, 1993, pp. 806-811.
10. Razdan, M.K., and Kuo, K.K., "Erosive Burning Study of Composite Solid Propellants by Turbulent Boundary-Layer Approach," *AIAA Journal*, Vol. 17, No. 11, 1979, pp. 1225-1233.
11. Lenior, J.M., and Robillard, G., "A Mathematical Method to Predict the Erosive Burning Effect in Solid Rockets," *6<sup>th</sup> International Symposium on Combustion*, Reinhold, NY, 1957.
12. Mukunda, H.S., and Paul, P.J., "Universal Behavior in Erosive Burning of Solid Propellants," *Combustion and Flame*, Vol. 109, 1997, pp. 224-236.
13. McDonald, Brian A., and Menon, Suresh, "Direct Numerical Simulation of Solid Propellant Combustion in Crossflow," *Journal of Propulsion and Power*, Vol. 21, No. 3, 2005, pp. 460-469.

## REFERENCES (CONT)

14. Kennedy, C.A., and Carpenter, M.H., "Comparison of Several Numerical Methods for Simulation of Compressible Shear Layers," *NASA Technical Paper 3438*, Langley Research Center, December 1997.
15. Gordon, S., and McBride, B.J., "Computer Program for Calculation of Complex Chemical Equilibrium Compositions, Rocket Performance, Incident and Reflected Shocks, and Chapman-Jouguet Detonations," NASA SP 273, 1971.
16. Poinso, T.J., and Lele, S.K., "Boundary Conditions for Direct Simulations of Compressible Viscous Flows," *Journal of Computational Physics*, Vol. 101, 1992, pp. 104-129.
17. Cazan, R. and Menon, S., "Direct Numerical Simulation of Sandwich and Random-Packed Propellant Combustion," *39<sup>th</sup> AIAA/ASME/SAE/ASEE Joint Propulsion Conference*, AIAA 2003-5082, July 2003.
18. A. Hegab, Jackson, T. L., Buckmaster, J., and Stewart, D.S., "Nonsteady Burning of Periodic Sandwich Propellants with Complete Coupling between the Solid and the Gas Phase," *Combustion and Flame*, Vol. 125, 2001, pp. 1055-1070.
19. Sutherland, James C., and Kennedy, Christopher A., "Improved Boundary Conditions for Viscous, Reacting, Compressible Flows," *Journal of Computational Physics*, Vol. 191, 2003, pp. 502-505.
20. Furfaro, James A., "Erosive Burning Study Utilizing Ultrasonic Measurement Techniques," *39<sup>th</sup> AIAA/ASME/SAE/ASEE Joint Propulsion Conference and Exhibit*, AIAA 2003-4806, July 2003.

## NOMENCLATURE

$a$	= Burning Rate Law Constant
$D_{hyd}$	= Hydraulic Diameter
$D_{ref}$	= Reference diameter
$E_a$	= Activation Energy
CFD	= Computational Fluid Dynamics
CP	= Center Perforated Propellant Grain
$G$	= Mass flux function
$M$	= Mach Number
$M_{sh}$	= Shear Mach Number (defined variable)
$n$	= Burning Rate Exponent
$P$	= Gas Pressure
$Pr$	= Prandtl Number
$r$	= Burning Rate
$r_o$	= Base Burning Rate
$Re_D$	= Reynolds Number
$Re_i$	= Injection Reynolds Number
$R_u$	= Universal Gas Constant
$T_{surf}$	= Propellant Surface Temperature
$U_m$	= Reference axial velocity
$u$	= Axial Velocity Component
$v$	= Normal Velocity Component
$\alpha$	= Thermal Diffusivity
$\lambda$	= Momentum ratio (blowing wall)
$\lambda_{NB}$	= Momentum ratio (non-blowing wall)
$A_{EB}$	= Erosive burning scaling function
$\mu$	= Molecular Viscosity
$\gamma$	= Skin friction coefficient
$\eta$	= Mass flux factor
$\rho_g$	= Gas Density
$\rho_p$	= Solid Propellant Density
$\tau_w$	= Wall shear stress (blowing wall)
$\tau_{w-NB}$	= Wall shear stress (non-blowing wall)

## INITIAL DISTRIBUTION LIST

		<u>Copies</u>
Weapon Systems Technology Information Analysis Center Alion Science and Technology 201 Mill Street Rome, NY 13440	Ms. Perry E. Onderdonk <a href="mailto:ponderdonk@alionscience.com">ponderdonk@alionscience.com</a>	Electronic
Defense Technical Information Center 8725 John J. Kingman Rd., Suite 0944 Fort Belvoir, VA 22060-6218	Mr. Jack L. Rike <a href="mailto:jrike@dtic.mil">jrike@dtic.mil</a>	Electronic
RDMR		Electronic
RDMR-CSI		Electronic
RDMR-SER,	Mr. Kevin M. James <a href="mailto:kevin.m.james@us.army.mil">kevin.m.james@us.army.mil</a>	Electronic
RDMR-WDP-M,	Dr. Robert R. Little <a href="mailto:robert.r.little@us.army.mil">robert.r.little@us.army.mil</a> Dr. Brian A. McDonald <a href="mailto:brian.mcdonald8@us.army.mil">brian.mcdonald8@us.army.mil</a>	Electronic Electronic
RDMR-WDP-P,	Mr. Philip Haberlen <a href="mailto:philip.a.haberlen@us.army.mil">philip.a.haberlen@us.army.mil</a>	Electronic
RDRL-WMD-B,	Dr. Michael J. Nusca <a href="mailto:nusca@arl.army.mil">nusca@arl.army.mil</a>	Electronic
AMSAM-LI,	Ms. Anne C. Lanteigne <a href="mailto:anne.lanteigne@us.army.mil">anne.lanteigne@us.army.mil</a>	Electronic
SFAE-MSL-AM-TP,	Mr. Roanld Adkins <a href="mailto:ron.adkins@us.army.mil">ron.adkins@us.army.mil</a>	Electronic